Global variable-resolution simulations of extreme precipitation over Henan, China in 2021 with MPAS-Atmosphere v7.3

Zijun Liu[1], Li Dong[1,2], Zongxu Qiu[3], Xingrong Li[3], Huiling Yuan[4], Dongmei Meng[5], Xiaobin Qiu[6], Dingyuan Liang[7], and Yafei Wang[8]

[1]Department of Earth and Space Sciences, Southern University of Science and Technology, Shenzhen, Guangdong, China
[2]Academy for Advanced Interdisciplinary Studies, Southern University of Science and Technology, Shenzhen, Guangdong, China
[3]Shenzhen National Climate Observatory, Shenzhen, Guangdong, China
[4]School of Atmospheric Sciences; Key Laboratory of Mesoscale Severe Weather/Ministry of Education, Nanjing University, Nanjing, Jiangsu, China
[5]Tianjin Meteorological Bureau, Tianjin, China
[6]Tianjin Key Laboratory for Oceanic Meteorology, Tianjin Institute of Meteorological Science, Tianjin, China
[7]Division of Environment and Sustainability, The Hong Kong University of Science and Technology, Hong Kong, China
[8]The Institute of Atmospheric Physics, Chinese Academy of Sciences, Beijing, China

Correspondence: Li Dong, dongl@sustech.edu.cn

Abstract. A historic rainstorm occurred over Henan, China in July 2021 ("7.20" extreme precipitation event), resulting in significant human casualties and socio-economic losses. A global variable-resolution model (MPAS-Atmosphere v7.3) was employed to simulate this extreme precipitation event ~~by bridging the hydrostatic and non-hydrostatic scales together.~~ . A series of simulations have been done at both quasi-uniform (60km and 15km) and variable-resolution ~~meshes~~ (60-15km and 60-3km) meshes from hydrostatic to non-hydrostatic scale with two parameterization scheme suites. For the 48-hour peak precipitation duration (07/20-07/22), the 60-3km variable-resolution simulation coupled with the scale-aware convection-permitting parameterization scheme suite stands out ~~predominately~~ predominatly among other simulation experiments as it reproduces this extreme precipitation event most accurately ~~, in terms of both the intensity and location of the peak precipitation.~~ . At 15-km resolution, the 60-15km variable-resolution simulation achieves comparable forecasting skills as the 15-km quasi-uniform simulation, but at a much reduced computing cost. In addition, ~~at 15-km resolution,~~ we found that the default mesoscale suite generally outperforms the convection-permitting suite at 15-km resolution as simulations coupled with convection-permitting suite missed the ~~3rd~~ third peak of this extreme precipitation event while the mesoscale suite did not. ~~This implies that, when the resolution of the refined region is coarser than the cloud-resolving scale, the convection-permitting parameterization scheme suite does not necessarily work better than the default mesoscale suite, but once the refined mesh is close to the cloud-resolving scale, the convection-permitting suite becomes scale aware such that it can intelligently distinguish the convective precipitation and grid-scale precipitation, respectively. Finally, it is found that the large-scale wind field plays a vital role in affecting extreme precipitation simulations since it primarily influences the transport of the water vapor flux thereby altering the prediction of the precise peak precipitation location.~~ Furthermore, it is found that the large-scale circulation plays a critical role in the peak precipitation simulations at 15km resolution, via influencing the simulated low-level wind. During the second peak precipitation period, simulations with the convection-permitting parameterization scheme suite at 15km resolution generate

a prominent low-level easterly component wind bias, which is largely attributed to the excessively evaporative cooling in the lower troposphere. This study further reveals that at 15km resolution the diabatic heating from the grid-scale precipitation accounts more for the low-level wind bias than the convective-scale precipitation. Given two different cloud microphysics schemes, namely Thompson and WSM6 schemes, are used in the convection-permitting and default mesoscale parameterization scheme suites respectively, these microphysics schemes are found to be the primary contributor to the low-level wind simulation bias.

1 Introduction

From July 17 to 22, 2021, a historic rainstorm occurred in Henan province of China ("7.20" extreme precipitation event), with a maximum hourly precipitation of 201.9mm. This rainstorm caused devastating urban flooding in Henan, resulting in 292 fatalities, 47 missing persons, and a direct economic loss of 53.2 billion yuan (Yin et al., 2021)(Yin et al., 2021; Rao et al., 2022). The rainstorm event occurred under the atmospheric circulation background of the abnormally enhanced western Pacific subtropical high (WPSH), which is displaced northward as well, and the dual typhoon presence (Typhoon Infa and Cempaka) (Xu et al., 2022). The main sources of water vapor for the present this heavy rain event can be attributed to three factors: the WPSH, Typhoons In-fa and Cempaka (Nie and Sun, 2022). East China frequently experiences summer extreme precipitation event such as the "7.20" event studied here due to East Asian Monsoon, tropical cyclones and mesoscale convective vortex (Ding and Johnny CL, 2005; Lonfat et al., 2004; Houze Jr, 2004). Previous studies have proposed numerous mechanisms for the occurrence and development of extreme precipitation events in eastern China. The subtropical high over the northwest Pacific is a key system affecting the East Asian summer monsoon and typhoons in the northwest Pacific region, which provides a possibility for seasonal prediction of the East Asian summer monsoon(Wang et al., 2013). The record-breaking Meiyu in the Yangtze River Basin in 2020 was characterized by a wide meridional rain belt with abundant precipitation and high frequency of occurrence of heavy rain. In addition, this long-lasting Meiyu season of 2020 is distinguished by an extended duration with an early onset and late retreat(Ding et al., 2021). Liu et al. (2020) pointed out that the summer extreme precipitation events are resulted from the sequential warm and cold Meiyu front that are regulated by the North Atlantic Oscillation. In addition, the The synoptic-system-related low-level jet (SLLJ) and boundary layer jet (BLJ) are closely related to heavy precipitation events in the coastal region of South China, and the interaction between these two jets has a critical impact on convective activity initiation (Du and Chen, 2019; Zhang and Meng, 2019). Zheng and Wang (2021) investigated the influence of the three main oceans on extreme precipitation in the Yangtze River Basin and found that sea surface temperature anomalies (SSTA) in the western North Atlantic in May could effectively predict precipitation anomalies in the Yangtze River Basin in June. With the global warming trend, the occurrence of the frequency of summer extreme precipitation events is on the rise and accurately predicting the duration and location of extreme precipitation events remains a significant challenge (Sun et al., 2016). Despite numerous studies have been done related to extreme precipitation simulations and rainfall data analysis, the forecasting performance for extreme precipitation events like the "7.20" rainstorm remains unsatisfactory, highlighting the need for improving the forecasting model to achieve sufficient prediction skills. (Chen et al., 2020; Sun et al., 2018; Liu et al., 2020).

The Model for Prediction Across Scales (MPAS-Atmosphere) is an advanced atmospheric forecasting model that has been widely applied to predict heavy rainfall, in particular, with the variable-resolution feature. Zhao et al. (2019) conducted MPAS experiments on the 2012 heavy rainfall event associated with Meiyu front in East Asia and pointed out that the model resolution has a significant impact on the strength and location of updrafts and precipitation. Additionally, Zhao et al. (2019) found that the convection-permitting Scheme is also suitable for global variable-resolution simulations. Xu et al. (2021) found that the low-resolution (60km) MPAS simulation overestimated the precipitation frequency (PF) of the Meiyu front precipitation, while underestimating the precipitation amount (PA) and intensity (PI), while, in contrast, the high-resolution (4km) MPAS simulation captured the diurnal cycle of PA well, even in the absence of typhoon influence. Furthermore, Cheng et al. (2023) compared MPAS global variable-resolution (MPAS-VR) with MPAS regional configuration (MPAS-RCM) and found that MPAS-VR outperformed MPAS-RCM in capturing the mean climate state, interannual variability, and extreme events of the East Asian summer monsoon. Moreover, the ~~comparison~~ difference between MPAS-VR and MPAS-RCM indicates that the former is a promising option for regional climate simulations as it can capture regional climate features with higher fidelity. These findings suggest that MPAS has the potential to provide more accurate predictions of heavy rainfall, especially with the global variable-resolution capability. The results also demonstrate the importance of selecting appropriate model resolution and parameterization scheme when predicting precipitation events.

To date, there has been relatively little work conducted on the simulation of extreme precipitation events in eastern China with the global variable-resolution MPAS model. This is a crucial research gap that needs to be filled as extreme precipitation events can have devastating consequences, leading to flash floods, landslides, and other severe weather-related disasters (Li et al., 2016; Zhai et al., 2005; Ding et al., 2008). Therefore, it is imperative to further investigate the performance of MPAS in simulating extreme precipitation events. This can be achieved through the analysis of its spatial and temporal resolution, parameterizations, and initialization methods (Liang et al., 2021; Zhao et al., 2016; Rauscher et al., 2013; Davis et al., 2016; Wang, 2022; Fowler et al., 2016). Furthermore, the evaluation of the performance of MPAS in simulating extreme precipitation events can help improve the accuracy and reliability of operational forecast of extreme precipitation events. In the present work, Section 2 introduces the data, MPAS model, physics parameterizations, and experimental design. Section 3 presents the evaluation of the MPAS experiments configured with different resolutions. Section 4 further analyzes the simulation performances with different ~~parametrization~~ parameterization scheme suites. The findings are summarized in Section 5.

2 Data and Methods

2.1 Observed and Reanalysis Data

Hourly surface observation data at 178 stations, including precipitation, temperature at 2m, and relative humidity, are provided by the National Meteorological Information Center of CMA (https://data.cma.cn/) to evaluate the simulated record-breaking heavy rainfall event that occurred during 20–21 July 2021 over Henan, China (32–37°N, 110–118°E). The hourly precipitation and wind field dataset from the European Centre for Medium-Range Weather Forecasts (ECMWF) Reanalysis (ERA5, 0.25°×0.25°) is used as a reference to evaluate the simulated distributions of precipitation and winds (https:

Table 1. Main Parameterization Schemes of MPAS

Parameterization	Mesoscale Scheme	Convection-Permitting Scheme
Convection	New Tiedtke	Grell-Freitas
Microphysics	WSM6	Thompson(non-aerosol aware)
Land surface	Noah	Noah
Boundary layer	YSU	MYNN
Surface layer	Monin-Obukhov	MYNN
Radiation, LW	RRTMG	RRTMG
Radiation, SW	RRTMG	RRTMG
Cloud fraction for radiation	Xu-Randall	Xu-Randall
Gravity wave drag by orography	YSU	YSU

//cds.climate.copernicus.eu/cdsapp#!/home). For comparison, the global forecast products starting from 00:00 UTC on 19 July 2021 at 0.25°horizontal resolutions are also utilized. All the above-mentioned data has undergone strict quality control.

2.2   MPAS-Atmosphere(MPAS-A) Model

90   The MPAS model (version 7.3) used in this study is a fully compressible non-hydrostatic model designed for weather and climate prediction (Skamarock et al., 2012; Skamarock and Klemp, 2008). MPAS utilizes C-grid staggering of prognostic variables and centroidal Voronoi meshes for sphere discretization. In MPAS, the grid refinement allows for a smooth transition from the coarse-mesh region of the globe to the fine-mesh region for the region of interest. MPAS uses the unstructured mesh based on spherical centroidal Voronoi tessellations (SCVTs), which allows the discretization of the sphere into either global

95   quasi-uniform mesh or variable-resolution mesh. The terrain-following hybrid coordinate is used for vertical discretization (Klemp, 2011). The MPAS atmospheric dynamical core solves the fully compressible non-hydrostatic equations of motion (Klemp et al., 2007). The vertical coordinate surfaces are progressively smoothed with height to eliminate the impact of small-scale terrain structures. The dynamical solver integrates the flux-form compressible equations using the split-explicit technique (Klemp et al., 2007). The third-order Runge-Kutta scheme is used for the basic temporal discretization, along with

100   the explicit time-splitting technique (Wicker and Skamarock, 2020), similar to that of the Weather Research and Forecasting (WRF) model (Skamarock and Klemp, 2008). The scalar transport scheme used by MPAS on its Voronoi mesh is explicated with the monotonic option used for all moist species (Skamarock and Gassmann, 2011). Extensive testing of MPAS simulations on idealized and realistic cases has verified that smooth transitions between the fine and coarse-resolution regions of the mesh do not significantly distort the atmospheric flow (Skamarock et al., 2012; Park et al., 2013).

105   MPAS incorporates two sets of built-in physical parameterization ~~schemes~~ scheme suites taken from the WRF model, specifically mesoscale (MS) suite and convection-permitting (CP) suite (Table 1). The ~~mesoscale physics~~ MS scheme suite has been tested for mesoscale resolutions (dx>~~10 km~~ 10km cell spacing)~~and is not appropriate for convective-scale simulations because~~
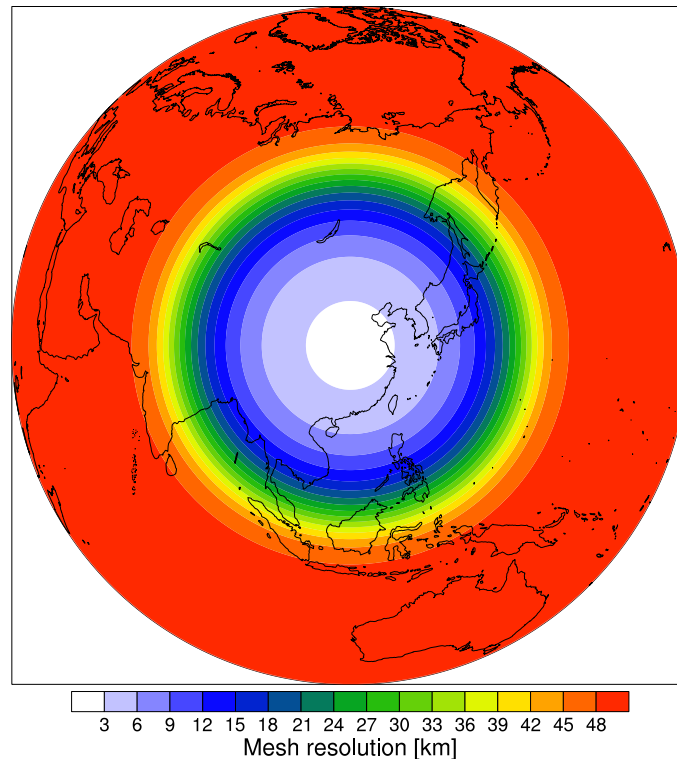
Figure 1. Global variable-resolution mesh size distribution in the 60-3km experiment

~~the Tiedtke convective scheme removes convective instability before the resolved-scale motions (convective cells) can respond to it. The convection-permitting physics~~, and the CP scheme suite is appropriate at spatial resolutions allowing for both ex-
110 plicitly resolved hydrostatic and ~~nonhydrostatic motions. It~~ non-hydrostatic motions. The CP scheme suite has been tested
for mesh spacings from several hundred kilometers down to several ~~km~~ kilometers in MPAS. The Grell-Freitas ~~convection~~
convective scheme of the convection-permitting ~~physics~~ suite transitions from a conventional parameterization of deep convec-
tion at hydrostatic scales (dx>~~10 km~~ 10km cell spacing) to a parameterization of shallow convection at cell spacings less than
10km (Fowler et al., 2016). This is the recommended suite for ~~any~~ MPAS simulations where convection-permitting meshes
115 (dx<10km) are employed. For instance, for the global variable-resolution mesh that bridges hydrostatic and non-hydrostatic
scales, the Grell-Freitas convection scheme is the optimal choice.

The New Tiedtke (NTD) scheme (Zhang et al., 2011; Bechtold et al., 2004, 2008, 2014) is similar to the Tiedtke scheme
(Tiedtke, 1989) used in the Regional Climate Model version4 (REGCM4) and the ECMWF model. The Grell-Freitas (GF)
scheme (Grell and Freitas, 2014) is an improved Grell-Dévényi scheme (Grell and Dévényi, 2002) that attempts to extend the
120 mesh resolution to cloud-resolving scales, as proposed by Arakawa et al. (2011). In particular, scale-aware parameterization
is essential for global simulations across hydrostatic and non-hydrostatic scales. Fowler et al. (2016) implemented the GF
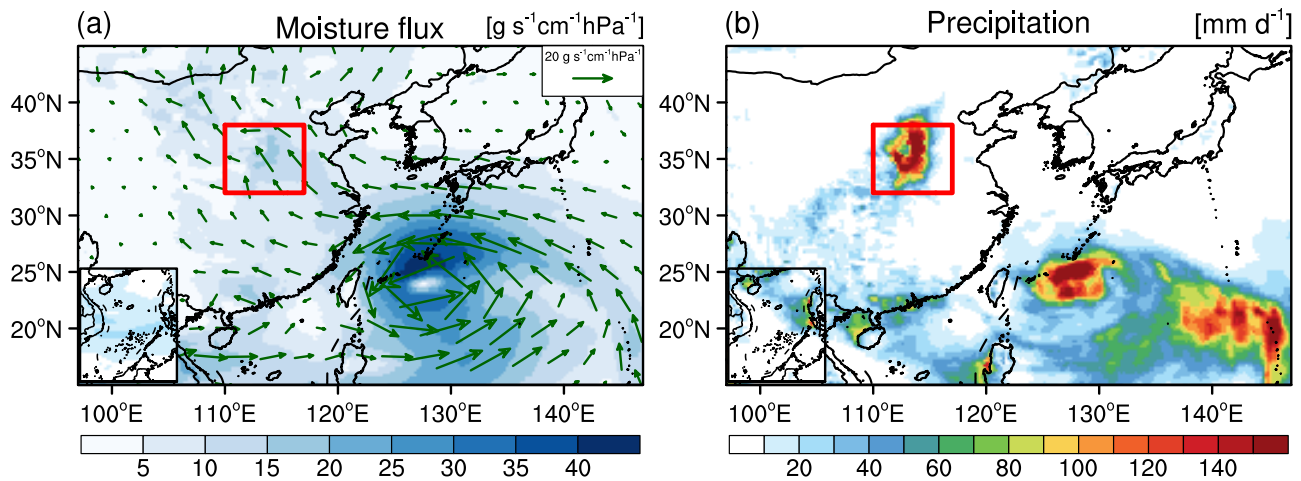
Figure 2. Background of the extreme precipitation event in Henan in July 2021. (a) Spatial distributions of moisture flux at 850-mb averaged from 00:00 UTC on July 19, 2021 to 00:00 UTC on July 23, 2021. The shading represents the intensity of water vapor flux. (b) Average daily precipitation (unit: mm/dy) from 00:00 UTC on July 19, 2021 to 00:00 UTC on July 23, 2021, derived from ERA5 hourly precipitation data. The red box denotes the target region.

scheme in MPAS and demonstrated that this scheme is functioned as a shallow convective scheme over the mesh refined region but a deep convection scheme over the coarse resolution region. As the horizontal resolution increases, subgrid-scale motions are resolved more accurately, leading to a decrease in the contribution of convective precipitation to the total precipitation and an increase in the contribution of grid-scale precipitation (Fowler et al., 2016). For cloud microphysics, the WRF Single-Moment 6-class (WSM6) scheme (Hong and Lim, 2006) is a one-moment prognostic parameterization with ice, snow and graupel, while the Thompson scheme (Thompson et al., 2008; Thompson and Eidhammer, 2014) includes hydrometeor species and graupel processes suitable for high-resolution simulations, both of which are bulk microphysical parameterizations. Two Boundary layer schemes are available in MPAS, namely, the Yonsei University (YSU) scheme (Hong et al., 2006; Hong, 2010) and the Mellor-Yamada-Nakanishi-Niino (MYNN) scheme (Nakanishi and Niino, 2006, 2009). Other available physical parameterization schemes in MPAS include the Noah land surface scheme (Chen and Dudhia, 2001), Monin-Obukhov surface layer and Rapid Radiative Transfer Model for GCMs (RRTMG) scheme (Iacono et al., 2000).

2.3 Numerical Experiments

Several experiments Several MPAS-A global simulations have been performed using MPAS on both quasi-uniform resolution meshes and variable-resolution meshes with two parameterization scheme suites (Table 2). All simulations have been conducted with 51 vertical levels up to 30km (Skamarock et al., 2019). Two quasi-uniform resolution meshes and two variable-resolution meshes are used in this study where the higher resolution is centered over the Henan province and covers the entirety of East China.Asia. The quasi-uniform mesh is characterized by a globally uniform distribution of mesh spacing,

Table 2. ~~Numerical~~ Description of the numerical experiments conducted and analyzed in this study. "MS" represents the Mesoscale scheme, while "CP" represents the convection-permitting scheme suite in Table 1. "~~U60km~~QU60km"("~~U15km~~QU15km") denotes the global quasi-uniform resolution of 60km(15km). "V15km"("V3km") represents the variable resolution with the grid spacing ranging from 60km to 15km(3km) ~~, which is confined to~~ with the ~~area~~ refined region illustrated in Fig. 1.

	MPAS experiments					
	~~U60km~~QU60km.MS	~~U15km~~QU15km.MS	~~U15km~~QU15km.CP	V15km.MS	V15km.CP	V3km.CP
Scheme	MS	MS	CP	MS	CP	CP
~~Mesh resolution~~ Resolution	~~U60km~~ QU60km	~~U15km~~ QU15km	~~U15km~~ QU15km	V15km	V15km	V3km
Num. of cells	163,842	2,621,442	2,621,442	535,554	535,554	835,586
Timestep (s)	90	60	60	60	60	20
Cost (CPU h)	1,289	2,316	2,528	571	726	3,120
Storage (TB)	0.3	1.5	1.6	0.4	0.4	0.6

~~whereas the variable-resolution mesh employs a high-resolution mesh in the refined region, supplemented by a transitional~~
~~zone that facilitates a seamless transition between the fine- and coarse-resolution meshes.~~ The two quasi-uniform meshes have grid spacing of ~~approximately~~ quasi-uniform 15km(~~U15km~~QU15km) and 60km(~~U60km~~QU60km), respectively. The two variable-resolution meshes feature a circular high-resolution region centered over East China. Fig. 1 shows the exact mesh ~~size distribution of the 60-3 km~~ resolution of the 60-3km variable-resolution mesh (V3km) that has a refined region with grid spacing of approximately ~~3 km~~ 3km with the mesh spacing gradually increasing through a transition zone to approximately ~~60 km~~ 60km for the rest of the globe~~(Fig. 1). .~~. The other variable-resolution mesh ~~has a similar mesh~~ (60-15km) configuration ~~has similar~~ structure but with ~~a~~ the mesh spacing of 15km (V15km) over the refined region ~~with the mesh spacing~~ gradually increasing to 60km ~~.~~ over the coarse region. It is noteworthy that the number of cells of the QU15km and V15km experiments are 2,621,442 and 535,554, respectively, while the number of cells of the V3km experiment is 835,586 (Table 2). The distinct numbers of cells will impact the computational and storage requirements for each experiment directly, despite the different timestep in the V3km experiment. The execution of a single QU15km.CP and V3km.CP experiment involves computational demands of 2,528CPU h and 3,120CPU h, along with storage requirements of 1.6TB and 0.6TB, respectively. Due to extensive computational and storage requirements, particularly for the QU15km and V3km experiments, we opted for a single-member ensemble in this study.

To simulate the heavy precipitation event that occurred during 20–21 July 2021 over Henan province, all the MPAS experiments were initialized at 00:00 UTC on 19 July 2021 to allow for appropriate spin-up time and the modeling results for 20–22 July 2021 are analyzed. The simulations were initialized using the analysis data at 0.25°horizontal resolution at 00:00 UTC on 19 July 2021 from the Global Forecast System (GFS) of the National Center for Environmental Prediction (NCEP), which is the same as what is used for the GFS forecast for that period. The sea surface temperature (SST) is also prescribed the same

as what is used by the GFS forecast for that period. This way, the MPAS simulations can also be compared against the GFS
forecast starting from 00:00 UTC on 19 July 2021.

3 Impacts of Resolution

Figure 2 illustrates the background of the extreme precipitation event that occurred in Henan in July 2021. Fig. 2a shows the
spatial distribution of water vapor transport flux during the event, with color shading representing the intensity of water vapor
transport. The region of July 21 extreme precipitation event is outlined by the red box(32°N-37°N, 110°E-120 °E). We selected
July 19 to July 23 to further specify the period of interest, with a particular focus on UTC times of July 20 and July 21, as there
were clear peaks during this period. During this time, Typhoon In-Fa and Typhoon Cempaka were associated with strong water
vapor transport, transporting moisture from the western Pacific and South China Sea to northern China. In the highlighted
area of Henan, a conspicuous convergence of water vapor was observed. The rainfall area during this period was generally
consistent with the area of maximum water vapor transport. ~~We are particularly interested in the precipitation distribution and
peaks in the Henan province during this period.~~ In the subsequent analysis, we partition the "7.20" extreme precipitation event
into two 24-hour periods, as mentioned by Rao et al. (2022), namely, the first peak on July 20th (from 20 July 00:00 to 21
July 00:00 UTC) and the second peak on July 21st (from 20 July 00:00 to 21 July 00:00 UTC), and precipitation during these
identified periods exceeds 80% of the total precipitation. This temporal segmentation facilitates a more detailed examination of
the distinct phases of the extreme precipitation event, allowing for a nuanced understanding of its evolution and characteristics.

3.1 First peak period

Figure 3 shows the spatial distributions of precipitation and wind at 850-mb averaged from 20 July 00:00 to 21 July 00:00
UTC from the simulations with global uniform and variable-resolution plus two parameterization ~~schemes~~suites. The mean
precipitation from the CMA stations and ERA5 reanalysis are also shown. The initiation time of the GFS forecast product co-
incides with the initiation time of the MPAS ~~experiment~~ experiments conducted in this study. Concentrated heavy rainfall zones
are evident in the CMA observations for the central and northern regions of Zhengzhou city, Henan province. Table 3 shows
the correlation ~~coefficient~~ coefficients (CC), root-mean-square error (RMSE) and mean bias (MB) of simulated and observed
precipitation. The results of the model simulations are presented in Fig. 3d-i. While precipitation exceeding 150 mm d^{-1} is
predicted in ~~the~~ Henan province, the spatial distribution of the precipitation pattern exhibits variations among the simulations.
The spatial correlation coefficient and RMSE of precipitation between the observation and the V3km.CP ~~simulations exhibits~~
simulation exhibit the greatest magnitude among all model simulations with a value of 0.51 and 11.78, respectively. Despite
having different mesh configuration, the simulated results of V15km.MS and ~~U15km~~QU15km.MS are similar, as well as for
the performance of V15km.CP and ~~U15km~~QU15km.CP. However, ~~U60km~~QU60km.MS failed to capture the heavy precipita-
tion occurring near Zhengzhou and incorrectly predicted the precipitation by locating the maximum precipitation area to the
southwest of Zhengzhou, due to the coarse grid resolution utilized in this simulation. Table 4 shows the correlation coefficients
(CC), root-mean-square error (RMSE) and mean bias (MB) of wind at 850-mb between the various simulations and ~~observed~~

CMA ERA5 reanalysis data. The correlation coefficient and RMSE of simulated and observed precipitation is in good agreement with the correlation coefficient of the simulated and observed simulated and ERA5 data wind at 850-mb, indicating a coherent response of precipitation to the atmospheric wind field. Interestingly, the observed maximum precipitation location is coincident with the apparent curving of the 850-mb wind vector, namely, the wind changes from southerly to southeasterly and then easterly, based on Fig. 3a. However, all simulations seem to fail to precisely reproduce the sharp curving of the horizontal wind, namely, most of the simulated wind vector merely turns from southeasterly to easterly instead. Hence, the mislocation of the simulated maximum precipitation is likely attributed to errors in the low-level wind simulations.
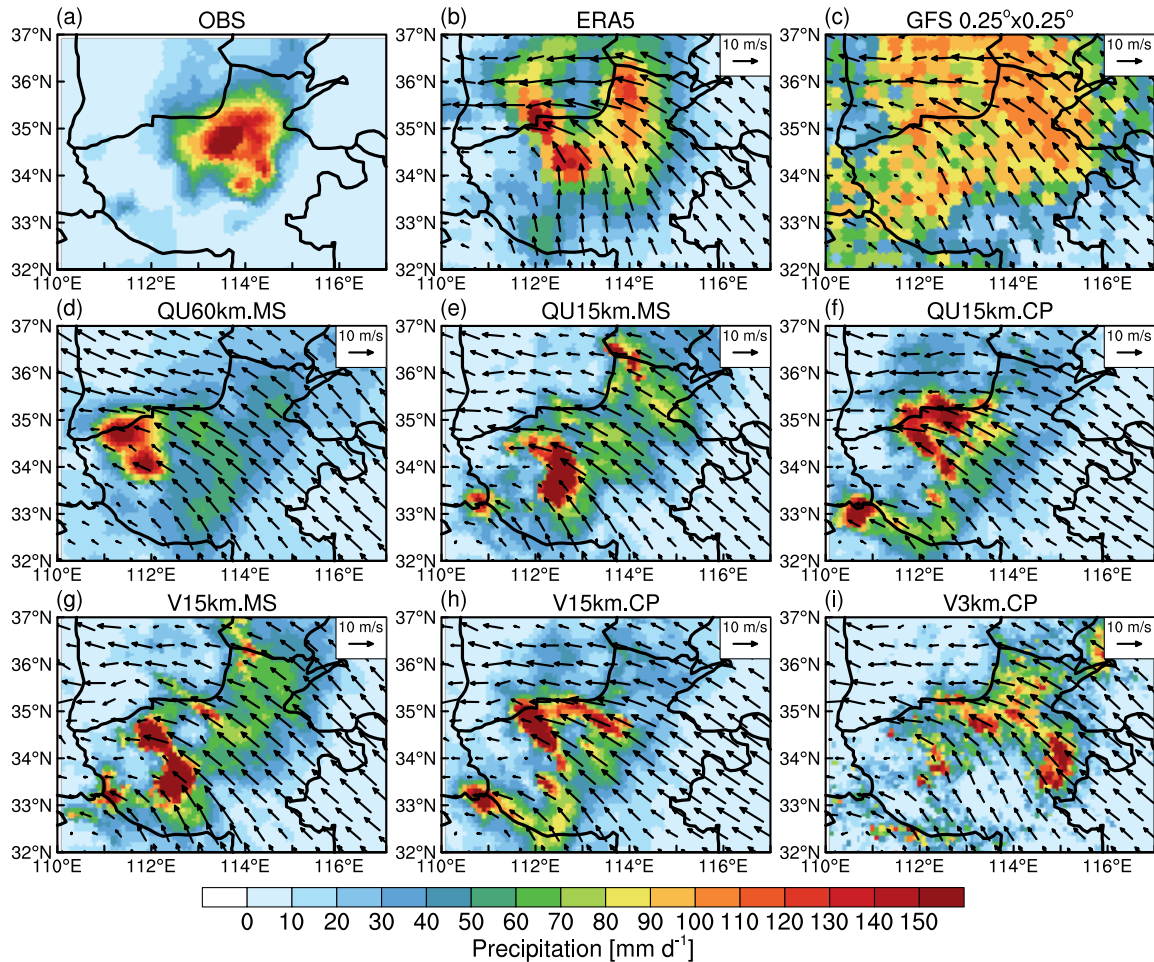
Figure 3. The observed mean precipitation from the CMA stations (a), ERA5 reanalysis (b), GFS 0.25° (c) are shown. Spatial distributions of precipitation and wind fields at 850 mb averaged from 20 July 00:00 to 21 July 00:00 UTC for the simulations with global quasi-uniform (60km, 15km) and variable (60-15km, 60-3km) resolutions, along with two parameterization schemes (MS : mesoscale scheme suite, CP : convection-permitting scheme suite) are shown in (d) through (i).

Table 3. The correlation coefficients (CC), root-mean-square error (RMSE) and mean bias (MB) of precipitation between the simulations and observed CMA data are listed below. The bold font in the table denotes statistical significance at the 95% confidence level based on the bootstrap analysis. "20 July pre." corresponds to the statistics (i.e., correlation coefficients, root-mean-square error and mean bias) between the simulations and OBS from 20 July 00:00 to 21 July 00:00 UTC of precipitation (Fig. 3). Similarly, "20 July zonal pre." represents the statistics of Fig. 5, while "21 July pre." represents Fig. 6, "21 July zonal pre." represents Fig. 8, "lat-time" represents Fig. 16, and "lon-time" represents Fig. 17.

	QU60km.MS	QU15km.MS	QU15km.CP	V15km.MS	V15km.CP	V3km.CP
20 July pre.	0.31, **31.12**, **-4.23**	**0.33**, **16.21**, **-3.12**	**0.38**, **15.83**, **-2.86**	0.31, **14.68**, **-3.01**	**0.35**, **15.22**, **-4.54**	**0.51**, **11.78**, **-4.92**
21 July pre.	**0.37**, **17.12**, **-9.94**	**0.32**, **16.19**, **-2.23**	0.07, **17.21**, **-7.42**	0.28, **17.89**, **-4.39**	0.06, **18.45**, **-8.44**	**0.62**, **12.23**, **-9.01**
20 July zonal pre.	**0.43**, **1.92**, **-0.84**	**0.78**, **1.43**, **-0.43**	**0.58**, **1.48**, **-0.53**	**0.71**, **1.56**, **-0.49**	**0.56**, **1.61**, **-0.37**	**0.86**, **0.72**, **+0.12**
21 July zonal pre.	**0.63**, **1.11**, **-1.23**	**0.43**, **2.32**, **-0.17**	0.22, **1.32**, **-1.87**	**0.51**, **2.04**, **-0.26**	0.14, **1.45**, **-1.42**	**0.89**, **0.32**, **-0.19**
lat-time (mm/h)	**0.42**, **0.73**, **-0.31**	**0.44**, **0.57**, **-0.24**	**0.40**, **0.81**, **-0.38**	**0.51**, **0.62**, **-0.24**	**0.42**, **0.74**, **-0.39**	**0.51**, **0.18**, **-0.09**
lon-time (mm/h)	**0.41**, **0.73**, **-0.35**	**0.51**, **0.62**, **-0.22**	**0.50**, **0.42**, **-0.19**	**0.50**, **0.88**, **-0.22**	**0.44**, **0.52**, **-0.20**	**0.58**, **0.23**, **-0.11**

Table 4. The correlation coefficients (CC), root-mean-square error (RMSE) and mean bias (MB) of wind at 850 mb between the various simulations and ERA5 data are listed below. The bold font in the table denotes statistical significance at the 95% confidence level based on the bootstrap analysis. "20 July U (V)" corresponds to the statistics between the simulations and ERA5 from 20 July 00:00 to 21 July 00:00 UTC of zonal (meridional) wind at 850-mb (Fig. 3). Similarly, "20 July U (V)" corresponds to the correlation coefficiens between the simulations and ERA5 from 21 July 00:00 to 22 July 00:00 UTC (Fig. 6).

	QU60km.MS	QU15km.MS	QU15km.CP	V15km.MS	V15km.CP	V3km.CP
20 July U	**0.32**, **0.88**, **-0.25**	0.31, **0.72**, **-0.22**	**0.35**, **0.91**, **-0.31**	**0.33**, **0.74**, **-0.20**	**0.38**, **0.89**, **-0.25**	**0.69**, **0.64**, **-0.03**
20 July V	**0.93**, **1.02**, **-0.14**	**0.89**, **0.88**, **-0.11**	**0.89**, **1.24**, **-0.21**	**0.86**, **0.83**, **-0.14**	**0.90**, **1.13**, **-0.22**	**0.93**, **0.83**, **-0.15**
21 July U	**0.29**, **1.35**, **-1.67**	**0.35**, **1.31**, **-1.45**	0.12, **3.04**, **-2.33**	0.27, **1.34**, **-1.44**	0.17, **3.09**, **-2.34**	**0.40**, **0.89**, **-0.23**
21 July V	**0.53**, **0.78**, **-0.12**	**0.68**, **0.45**, **-0.13**	**0.43**, **3.08**, **-2.45**	**0.63**, **0.43**, **-0.16**	**0.46**, **3.13**, **-2.46**	**0.64**, **0.54**, **-0.12**

To better illustrate the performance of simulations in terms of precipitation, Fig. 4 shows the differences between the simulations and observations averaged from 20 July 00:00 to 21 July 00:00 UTC. All simulations consistently underestimated the precipitation intensity near Zhengzhou and forecasted higher intensity in the western region of Henan incorrectly except for the V3km.CP simulation. It is worth noting that V3km.CP exhibited the least pronounced discrepancies from observation, with an underestimation of 40 mm d^{-1} near Zhengzhou. These discrepancies were also more dispersed compared to other simulations. The simulations of variable- and uniform- resolutions are generally consistent at the mesh of the same fine resolution. However, the variable-resolution approach can significantly reduce computing cost. The discrepancy of ~~U60km~~QU60km.MS from observation is the most pronounced among all simulations, which is consistent with the conclusion in Fig. 3.
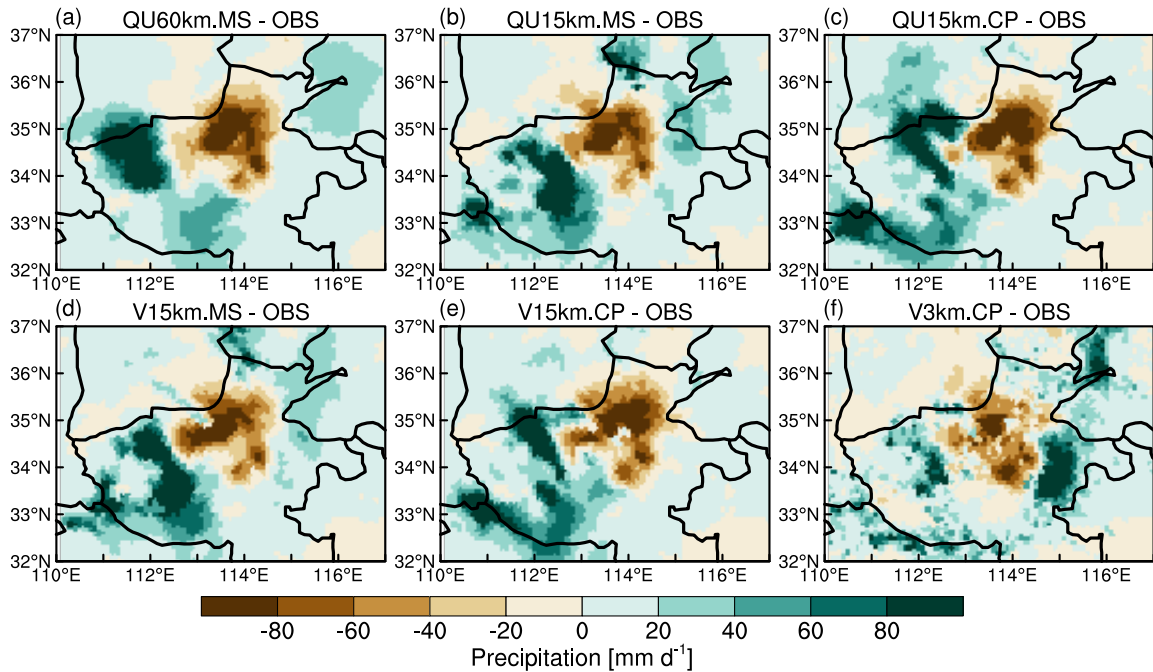
Figure 4. The difference of precipitation between simulations and CMA stations from 20 July 00:00 to 21 July 00:00 UTC.

In order to visually represent the change of observed and simulated precipitation intensity along longtitude over the peak precipitation region, we calculated the zonal distributions of precipitation averaged over the red-box region in Fig. 2 from 20 July 00:00 to 21 July 00:00 UTC as show in Fig. 5. Consistent with the previous conclusion, the V3km.CP simulation outperforms all other experimental configurations with ~~a correlation coefficient with observations~~ CC, RMSE and MB being 0.86, 0.72 and +0.12, respectively. Regarding 15km simulations, the variable-resolution simulation generally presents a peak precipitation slightly west of that simulated by the quasi-uniform simulation. Meanwhile, for both 15km variable-resolution simulation and 15km quasi-uniform simulation, the CP parameterization suite surpasses the MS suite by presenting greater maximum precipitation close to observed values. Finally, the quasi-uniform 60km simulation presents the least sufficient performance with an excessively low simulated precipitation peak value and incorrect zonal distribution. In summary, due to the outstanding resolution and matching parameterization scheme utilized, the V3km.CP exhibits the optimal forecasting skills. On the contrary, the ~~U60km~~ QU60km.MS shows the worst prediction performance. The utilization of the CP scheme in the simulations effectively captures the maximum values, given the convection-permitting scheme suite is scale aware in that it can dynamically compute resolved and ~~parameterized~~ convective precipitation according to different resolutions in the variable-resolution mesh.
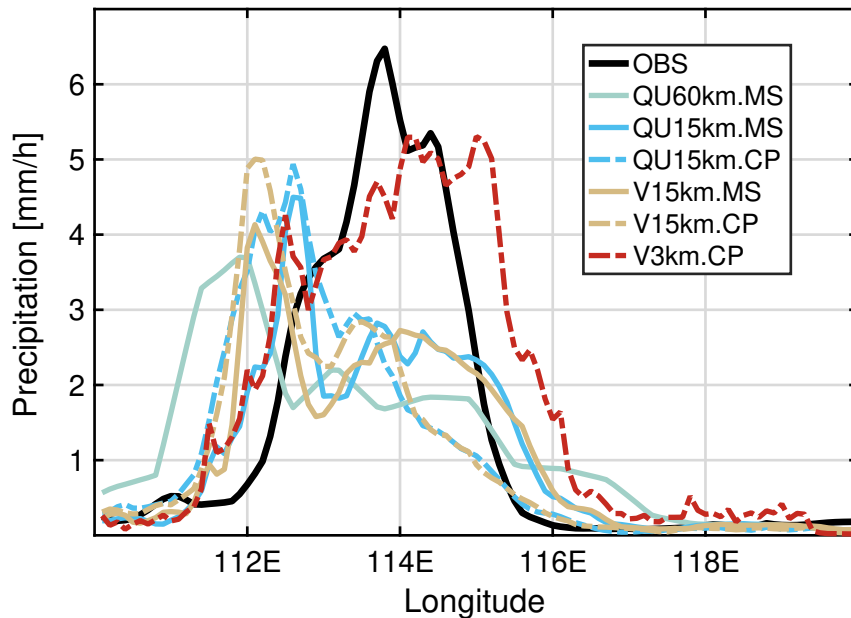
Figure 5. Zonal distributions of precipitation averaged from 20 July 00:00 to 21 July 00:00 UTC over Henan (denoted as the red box in Fig. 2) for the CMA station observations and the simulations with resolutions of 60, 15, and 3km.

3.2 Second peak period

Figure 6 shows the ~~comparison between observed and simulated precipitation~~, precipitation and wind among observation, ERA5 reanalysis, GFS and simulations, just same as Fig. ~~5~~ 3, except for the time period from 00UTC July 21 to 00UTC July 22. During this 24-hr period, the observed rainfall zone keeps moving northward and reaches northern Henan province indicated in Fig. ~~6a~~ 6a. Among all simulations, only V3km.CP correctly captures both the position and intensity of the precipitation, showing ~~a spatial correlation coefficient~~ the CC and RMSE of 0.62 ~~with the observations~~ and 12.23, respectively (Table 3). Generally, at 15km hydrostatic-scale resolution, with the same parameterization scheme suite being selected, the variable-resolution simulation results resemble the 15km quasi-uniform simulation results closely. Meanwhile, the two sets of parameterization suites, i.e., MS vs CP, turn out to have different impacts upon the simulated precipitation at 15km resolution. Specifically, the MS parameterization suite tends to give rise to two locations of simulated peak precipitation, i.e. one is over the North Henan province, just nearly identical to the observation. The other is over the Soutwest Henan province with even greater precipitation intensity. As for the CP parameterization suite, there is nearly none precipitation simulated over North Henan province. Instead, the simulated two precipitation bands are spread out over Southwest Henan province. In this sense, the MS suite seems superior to CP for this 24-hr simulation period at 15km resolution. This can be reflected from Fig. 7 as well. ~~However, all~~ As for the simulated 850-mb wind field ~~for the second 24-hr exhibit notably inferior performance when contrasted with those of~~, among all simulation experiments, the V3km.CP experiment exhibits a closer resemblance to ERA5. Nevertheless, the
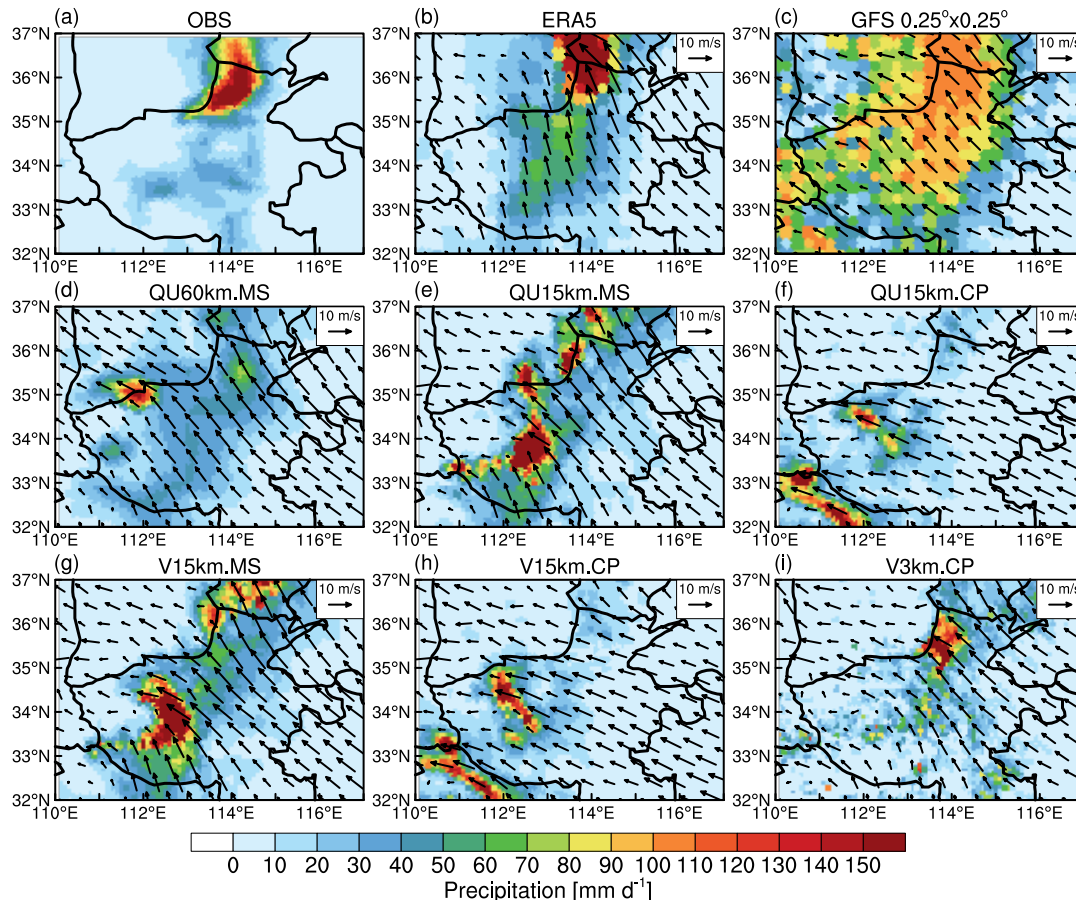
Figure 6. Same as Fig. 3, except for the average from 21 July 00:00 to 22 July 00:00 UTC.

performance of model simulations for this 24hr period is generally inferior to that of the first 24hr period. Table 4 reveals that, at 15km resolution of both quasi-uniform and variable-resolution mesh, the ~~first 24-hour simulations, specifically at the resolution of 15km(Table 4). Furthermore, Table 4 shows the U15km.CP and V15km.CP simulations of~~ simulated 850-mb wind ~~field are notably inferior to those achieved with U15km.MS and V15km. MS.~~ with the MS suite outperforms the CP

240   suite. This discrepancy is one of the contributing factors leading to the subpar performance of the CP scheme in this 24-hr precipitation simulation. It is very likely that the simulated wind field from MS and CP parameterization suites, respectively, plays a key role in governing the location of the simulated peak precipitation. Namely, the MS suite generates prevailing 850-mb southeasterly wind which tends to maintain the peak precipitation region over ~~North~~ north Henan province while shifting another peak precipitation region to Southwest Henan province. As for the CP suite, it seems to favor 850-mb ~~westerly~~ easterly

245   wind generation over Henan province such that the simulated peak precipitation region tends to shift further west and none peak precipitation is reproduced over North Henan province. The in-depth analysis upon the source of this simulation bias will
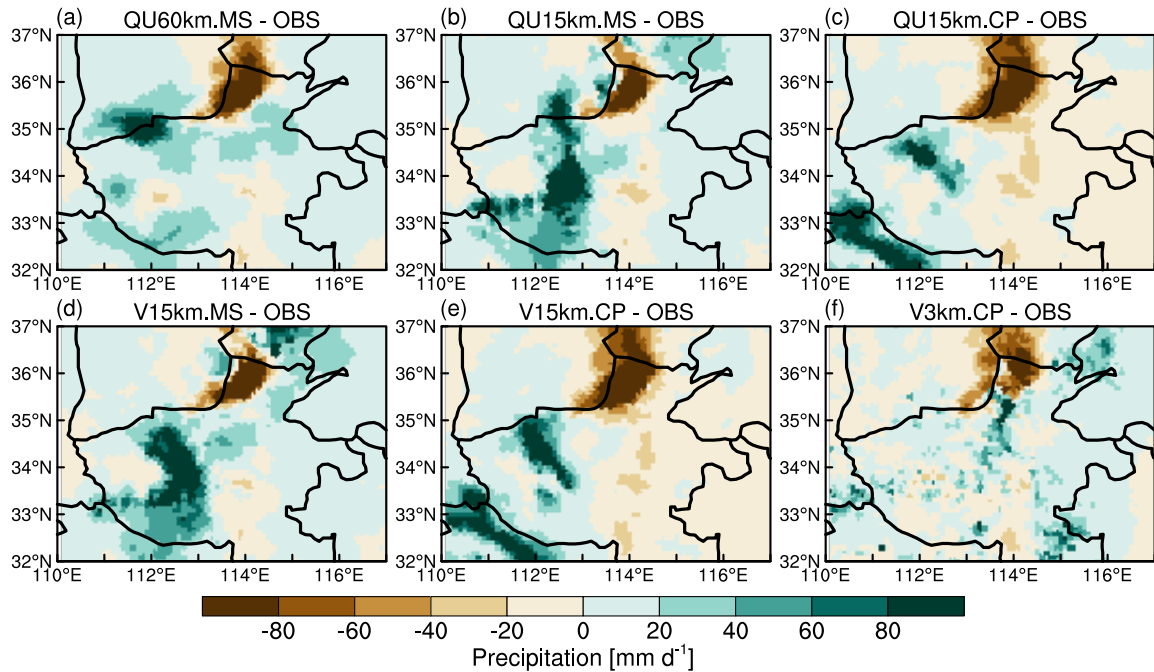
Figure 7. Same as Fig. 4, except for the average from 21 July 00:00 to 22 July 00:00 UTC.

be elaborated in the following paragraph. Once again, it is confirmed that the simulated low-level wind field plays a vital role in the peak precipitation simulations, in terms of both precipitation intensity and location.

The contents presented in Fig. 8 are consistent with those in Fig. 5, but represent the hourly average precipitation from 21 July 00:00 to 22 July 00:00 UTC. The observation indicates a weakening of the precipitation peak during this period (5mm/~~hr~~h), with the maximum precipitation value slightly shifting eastward to 114°E. Once again, for simulations at 15km resolution, regardless of variable-resolution or quasi-uniform mesh, it is found that the MS parameterization scheme suite outperforms CP scheme suite in terms of precipitation intensity simulation with the CP scheme suite predicting a precipitation intensity (3mm/~~hr~~h) far below the observed value (above 5mm/~~hr~~h). This is consistent with what Fig. ~~6~~ 6 depicts. As for 3km resolution, the variable-resolution simulation with CP parameterization scheme suite achieves the supreme performance, accompanied by a pattern correlation coefficient with observations being 0.89.

In order to figure out why the simulation at 15km with the CP suite tends to produce an easterly wind component anomaly relative to the MS suite during this 24hr period, we did further analysis to pursue the possible source error. Figure 9 shows the 850-250mb vertically averaged temperature anomaly from ERA5 and it clearly depicts that simulations with the CP suite generates a greater cooling anomaly (Fig. 9c and 9e) relative to the MS suite(Fig. 9a, 9b and 9d) . This cooling anomaly results in an intensified thickness shrinking within the 850-250mb air column for the simulations with the CP suite, which in turn leads to a local rise of the lower-tropospheric geopotential height, as shown in Fig. 10c and 10e. This local geopotential height
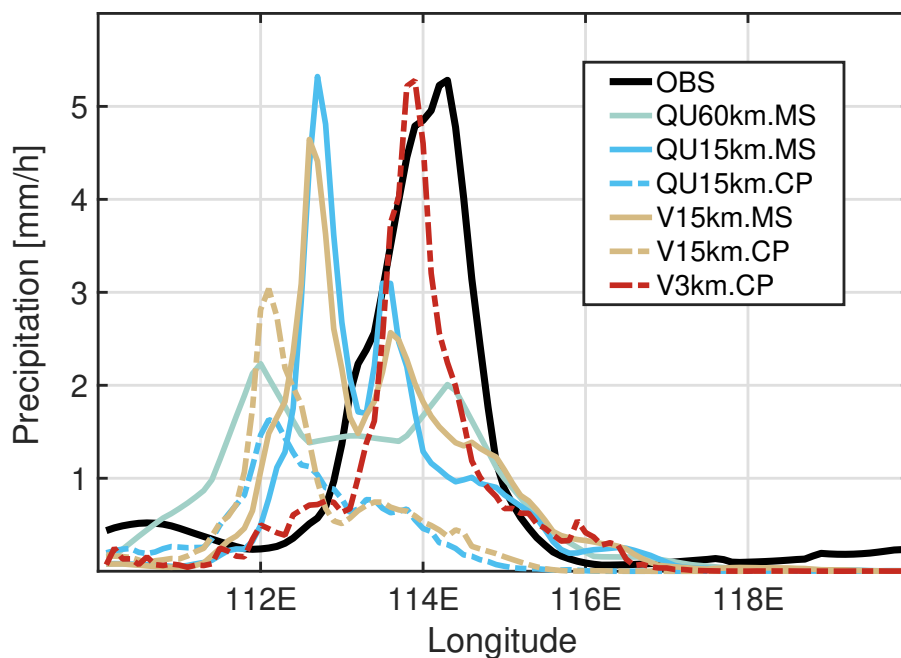
Figure 8. Same as Fig. 5, except for the average from 21 July 00:00 to 22 July 00:00 UTC.
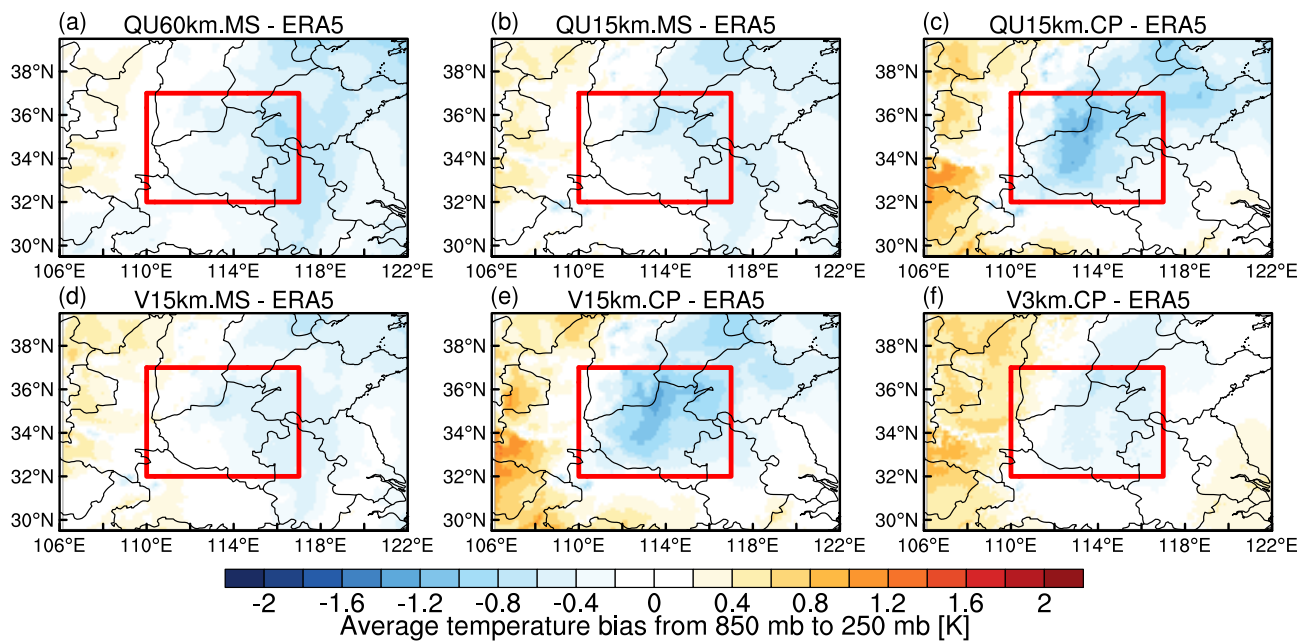
Figure 9. The difference of vertically averaged temperature from 850 mb to 250 mb between simulations and ERA5 from 21 July 00:00 to 22 July 00:00 UTC.
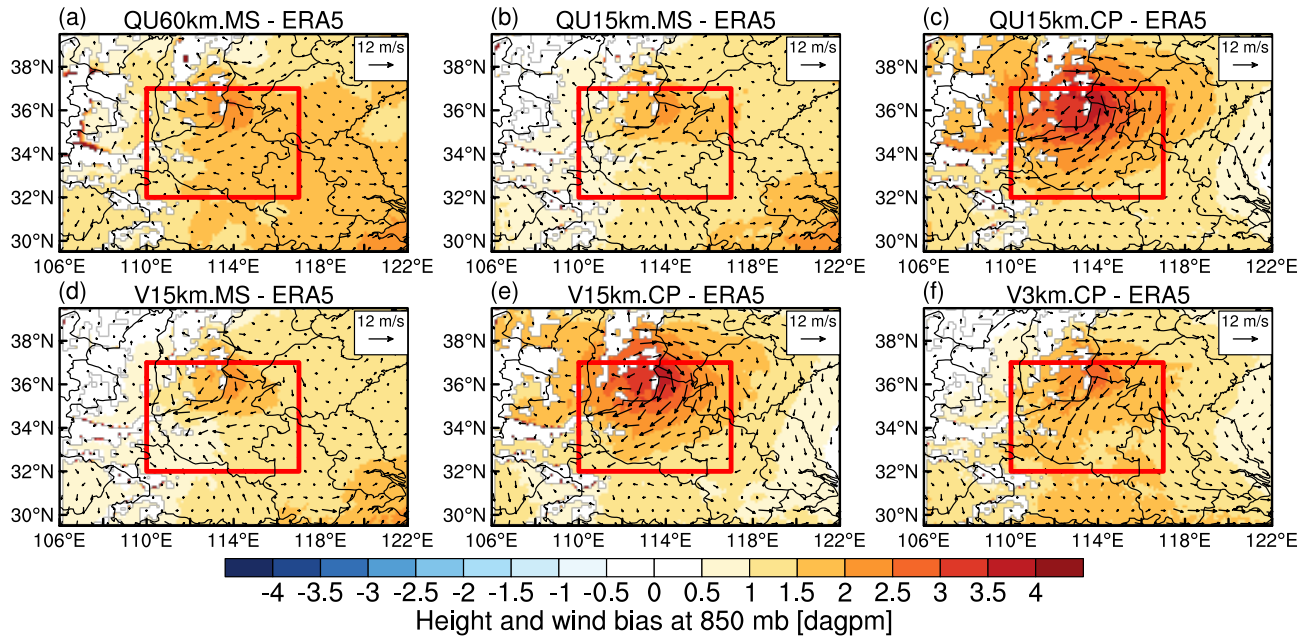
Figure 10. The difference of geopotential height and wind at 850 mb between simulations and ERA5 from 21 July 00:00 to 22 July 00:00 UTC.
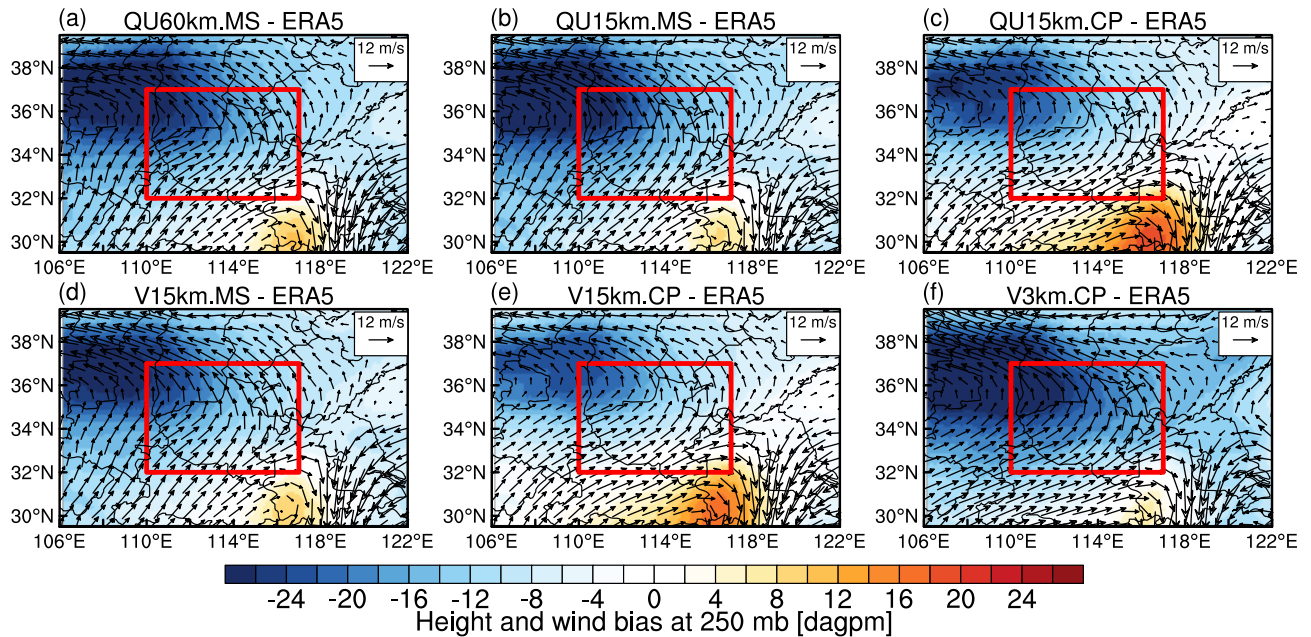
Figure 11. The difference of geopotential height and wind at 250 mb between simulations and ERA5 from 21 July 00:00 to 22 July 00:00 UTC.
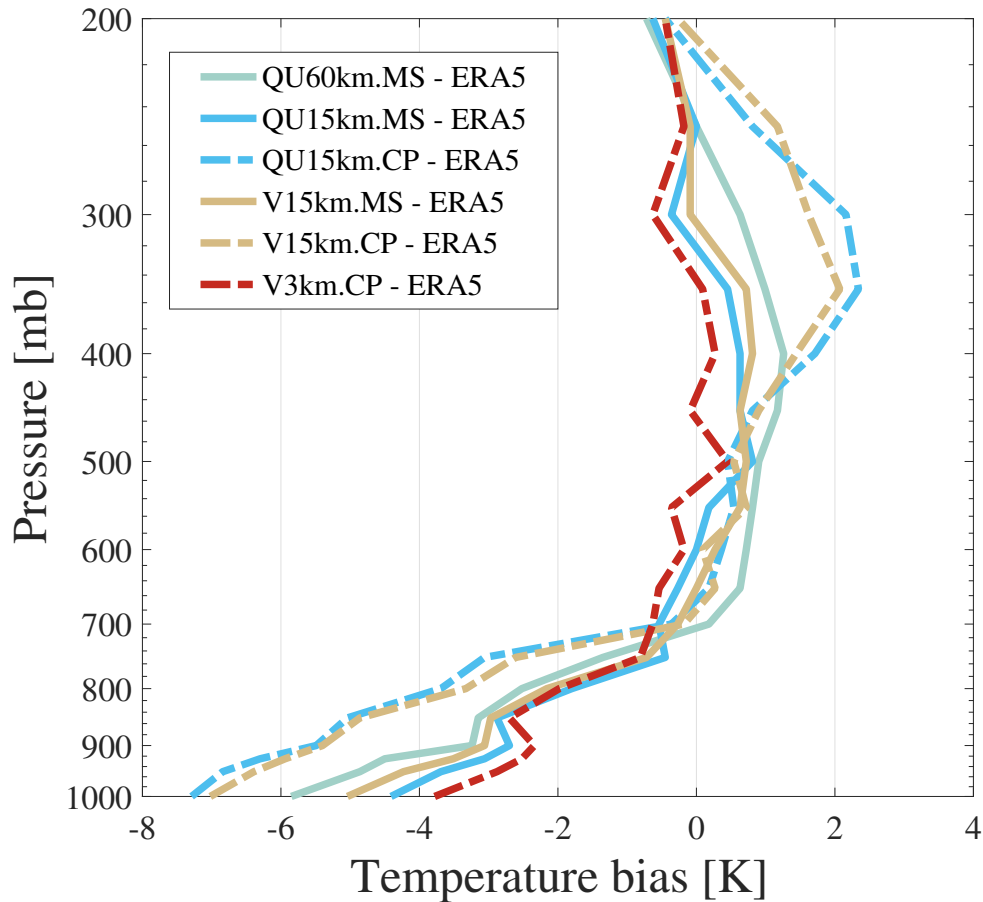
Figure 12. Vertical profiles of the averaged temperature difference between the simulation and ERA5 from 21 July 00:00 to 22 July 00:00 UTC. The averaged areas are denoted as the red boxes in Figure 2.

rise corresponds to an anticyclonic circulation anomaly which gives rise of an easterly wind anomaly for simulations with the CP suite relative to the MS suite.

265   Furthermore, Fig. 11 presents the geopotential height and wind anomaly changes over the upper troposphere, in response to the 850-250mb vertically averaged air column cooling effect. The evident 250-mb southwesterly anomaly flow over the outlined region is coincident with the cool-warm temperature gradient along the northwest-southeast diagonal (Fig. 13c and Fig. 13e), based on the thermal wind balance. In addition, it is observed that a local drop of 250-mb geopotential height is dominant over the outlined region for all simulations, where simulations at 15km resolution with the CP suite generates a

270   smaller magnitude of geopotential height drop relative to the MS suite. This can be attributed to the enhanced warming within the upper troposphere for simulations with the CP suite, as depicted in Fig. 12. In other words, given the anomalous cooling
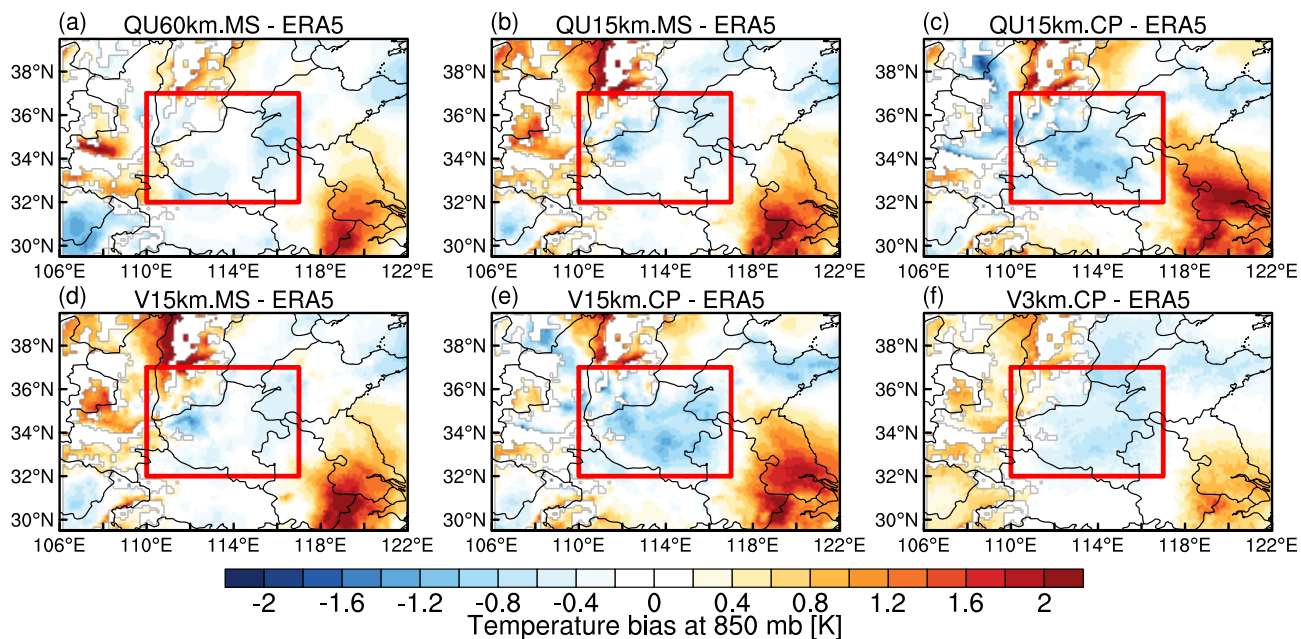
Figure 13. The difference of temperature at 850 mb between simulations and ERA5 from 21 July 00:00 to 22 July 00:00 UTC.

effect within the 850-250mb air column for simulations with the CP suite, the geopotential height at the top layer would drop due to the reduced air column thickness, however, at the same time the upper-level warming anomaly within the air column would offset this height drop such that the overall drop of 250-mb geopotential height would decrease in magnitude. Figure 12 clearly demonstrates that for simulations with the CP suite at 15km resolution there is an amplified cooling in the lower troposphere whereas an enhanced warming in the upper troposphere. This is very likely due to simulation bias of condensational warming in the upper troposphere and evaporational cooling in the lower troposphere. Further investigation of this diabatic heat bias will be presented in the coming section.

4 Impacts of Parameterization

4.1 Convective Precipitation and Grid-scale Precipitation

The ~~GF parameterization of convection utilizes a scaling factor, which is a quadratic function of the~~ moist processes and precipitation can be classified as implicitly represented using convective parameterization schemes (convective rain) or explicitly simulated using cloud microphysics parameterization schemes (grid-scale rain) (Fowler et al., 2016). The adaptability of mass-flux-based convective parameterization to function effectively across scales is illustrated by Arakawa and Wu (2013) through reducing the convective vertical eddy transport in proportion to the horizontal fraction of the grid box. Arakawa and Wu (2013) calculates

the vertical eddy transport $\overline{\omega'\psi'}$ as

$$\overline{\omega'\psi'} = (1-\sigma)^2(\overline{\omega'\psi'})_E, \qquad (1)$$

where ω is the vertical velocity, σ is the convective updraft fraction and $(\overline{\omega'\psi'})_E$ denotes the vertical eddy transport in the context of full quasi-equilibrium adjustment. Fowler et al. (2016) calculates the σ as

$$\sigma = \frac{\pi R^2}{A}, R = \frac{0.2}{\varepsilon}, \qquad (2)$$

where A represents the grid box area, and ε is an initial fractional entrainment rate pre-defined as $7\times10^{-5}\mathrm{m}^{-1}$. In QU60km and QU15km simulations, the calculation of σ is carried out using Eq. 2, resulting in values of 0.01 and 0.11, ~~to calculate convective and grid-scale precipitation over the coarse and refined mesh regions,~~ respectively. In V3km simulations, the value of σ transitions from 0.7 to 0 smoothly as the grid distance continually increases, whereas in V15km simulation, σ transitions from 0.11 to 0 as mesh resolutions changes from 15km to 60km(Fowler et al., 2016). For cloud microphysics shemes, as mentioned above, the WSM6 scheme in MS scheme suite and Thompson scheme in CP scheme suite are both bulk microphysical parameterizations and include water vapor, cloud water, rain, cloud ice, snow, and graupel.

Due to the exponential decay parameter, the Thompson scheme permits an increase in fall speed as resolution increasing. To demonstrate the scale-aware performance of the GF ~~cumulus~~ convective parameterization across various resolutions, which is embedded in the convection-permitting physics suite, we evaluate the performance of GF using quasi-uniform and variable-resolution meshes, which vary from hydrostatic (60km) to ~~nonhydrostatic~~ non-hydrostatic (3km) scales. Fig. 14 shows the spatial distribution of ~~parameterized~~ convective (upper four panels), resolved (medium four panels), and total (lower four panels) precipitation simulated by MPAS, averaged from 20 July 00:00 to 22 July 00:00 UTC. At the mesh resolution of ~~60 km,~~ 60km, in QU60km.MS simulation, the spatial distribution of total precipitation is mainly influenced by ~~parameterized~~ convective rain, whereas the spatial maximum of precipitation is influenced by ~~resolved~~ grid-scale rain. In contrast, at the mesh resolution of 3km, both the spatial distribution of total precipitation and the extreme precipitation are primarily influenced by ~~resolved~~ grid-scale rain, with the impact of ~~parameterized~~ convective rain being negligible. Since the scale-aware GF convection scheme performs as a conventional deep convective scheme over the coarse region and as a shallow convective scheme over the refined region, with the increasing mesh resolution, the grid-scale precipitation becomes dominant in the total precipitation relative to the convective precipitation.

At the mesh resolution of 15km, the contribution of ~~parameterized rain and resolved rain~~ convective precipitation and grid-scale precipitation to total precipitation lies between the performances of ~~U60km~~QU60km.MS and V3km.CP. ~~Furthermore, at the same resolution of 15km, the performances of mesoscale scheme suite and convection-permitting scheme suite exhibit significant differences. Specifically, the total precipitation of~~ Here we analyze the impact of the scaling factor $(1-\sigma)^2$ upon the updraft mass flux. In V15km.CP simulation, the value of σ in the refined region is 0.11, with $(1-\sigma)^2$ equal to 0.79. The large value of this $(1-\sigma)^2$, in conjunction with $(\overline{\omega'\psi'})_E$, predominantly governs the vertical eddy transport $(\overline{\omega'\psi'})$, leading to the evident convective precipitation shown in Fig 14c. In contrast, in V3km.CP simulation, the value of σ in the refined region is 0.7, with $(1-\sigma)^2$ equal to 0.09. Here, the small value of $(1-\sigma)^2$ primarily minimizes the vertical eddy transport
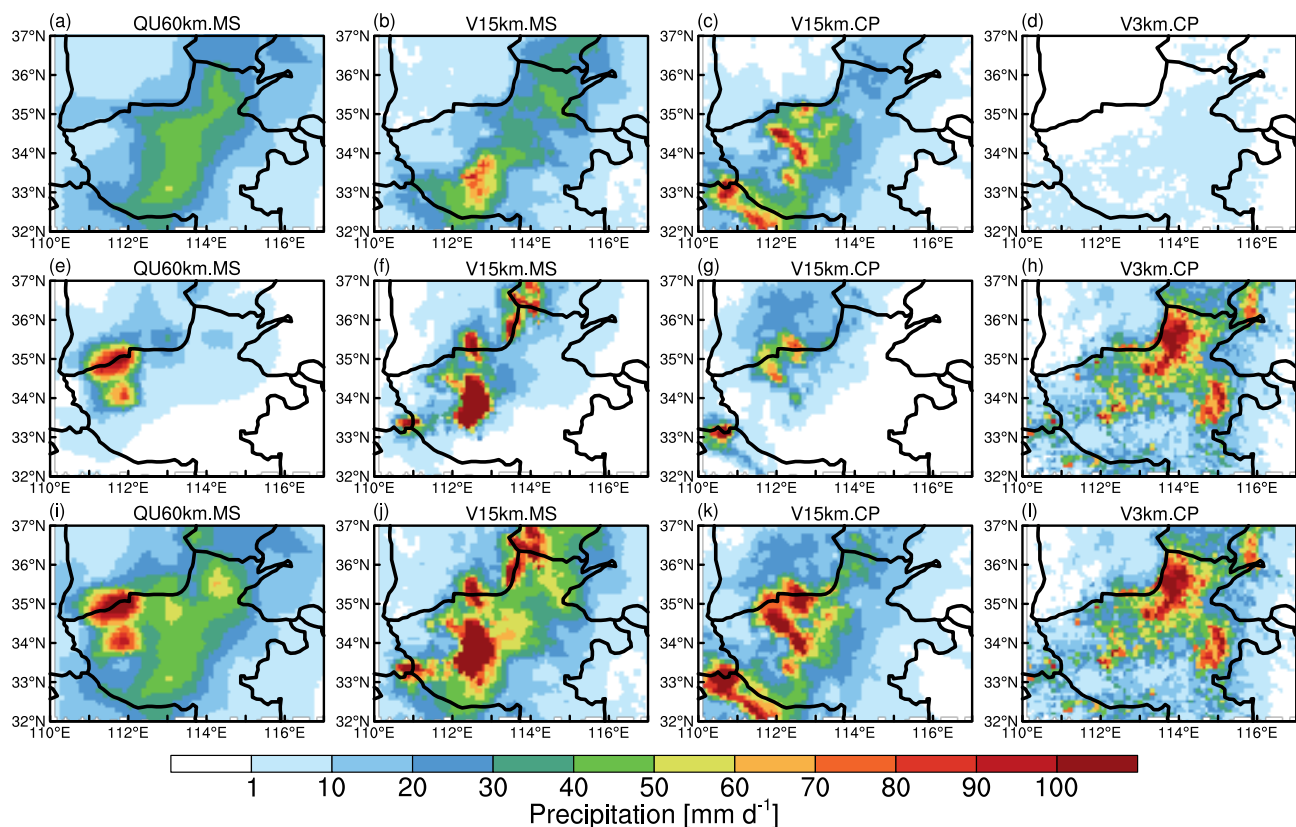
Figure 14. Spatial distribution of convective (upper four panels), grid-scale (medium four panels), and total (lower four panels) precipitation averaged from 20 July 00:00 to 22 July 00:00 UTC over Henan province from the simulations with resolutions of 60, 15, and 3km, respectively.

$(\overline{\omega'\psi'})$, resulting in almost no convective precipitation in Fig 14d. In V15km.MS ~~is dominated by resolved rain, which is mainly~~ ~~generated by cloud microphysics, while~~ simulation, where the mass-flux-based convective scheme NTD is used, equivalent to the GF scheme with σ equal to 0, convective rain is closer to that in QU60km.MS, despite an erroneous precipitation center over southwest of Henan province. Regarding total rain, the V15km.~~CP is dominated by parameterized rain, which is mainly~~ ~~generated by convective activities.Therefore, these experiments with different parameterization schemes confirm that the GF~~ ~~convection parameterization scheme , utilized by the convection-permitting parameterization scheme suite~~ MS simulation correctly predicts high precipitation center in northern Henan compared to V15km.CP, ~~shows the scale-aware performance.~~ although there are still numerous incorrect predictions in the southwestern region. In addition to different contributions from convective precipitation, the contribution to total rain from grid-scale rain generated by microphysics parameterization in both V15km.MS and V15km.CP remains significant. We found that the discrepancy between these V15km.MS and V15km.CP arises from the distinct microphysics schemes generating different grid-scale precipitation, ultimately resulting in disparate
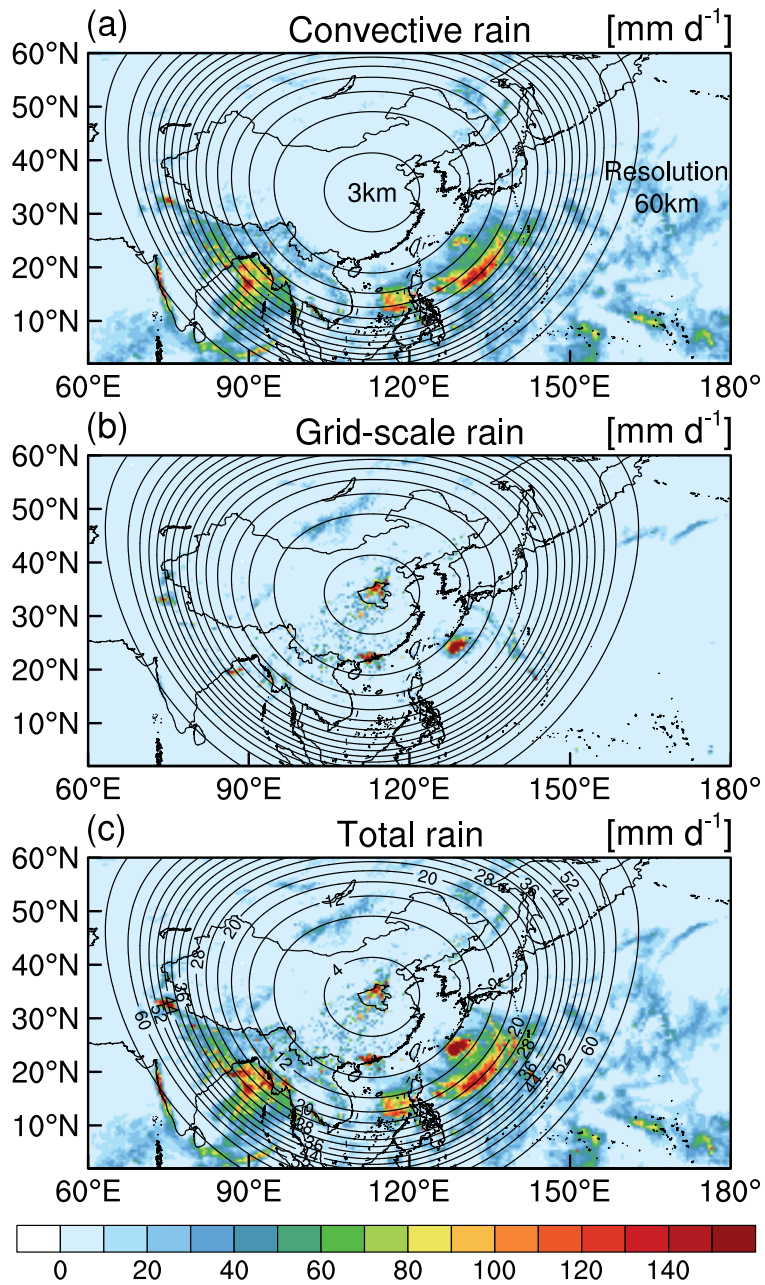
Figure 15. Spatial distribution of averaged convective, grid-scale, and total precipitation from 20 July 00:00 to 22 July 00:00 UTC from the V3km.CP simulation. The solid black line represents the grid resolution from 64km to 4km by 4km, and the label "3km"("60km") in the Fig. 15a denotes a horizontal resolution of 3km(60km) within the specified region.
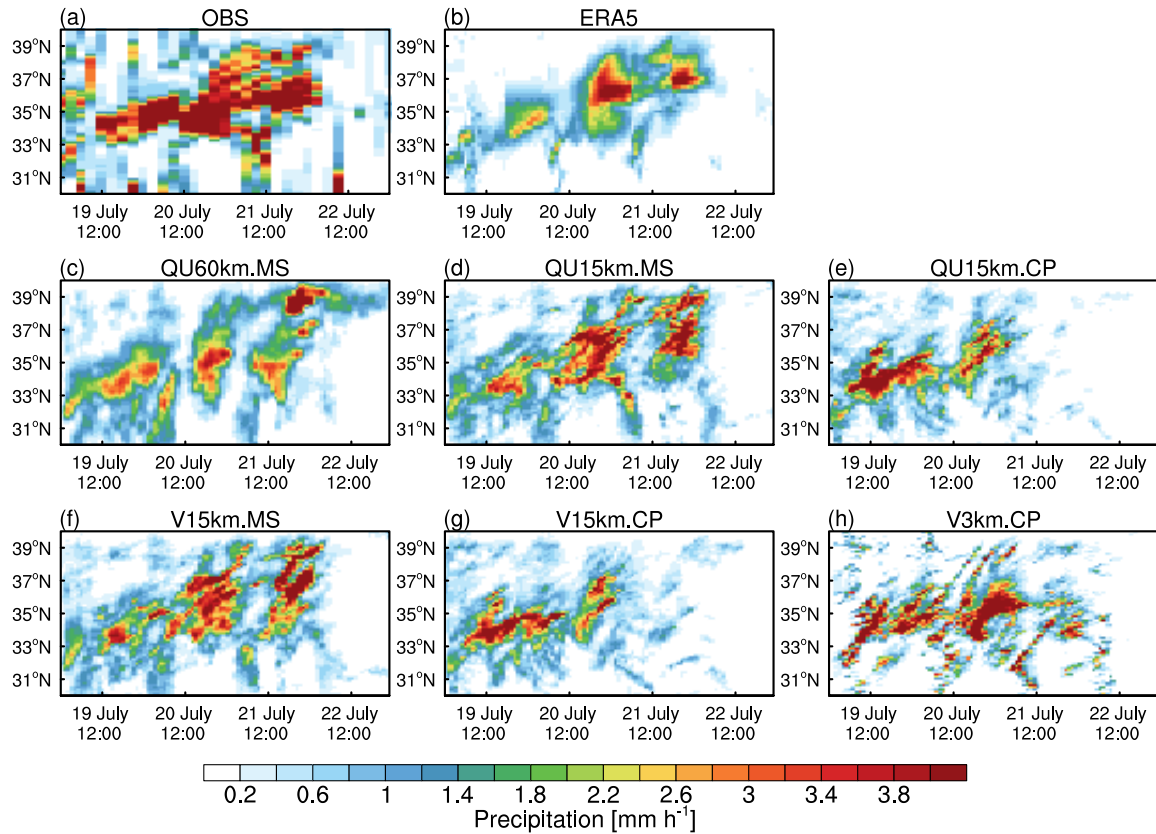
Figure 16. Time–Latitude cross section of precipitation over Henan province (30°N–40°N, 110°E–130°E) from the CMA station observations and the simulations with global uniform and variable-resolution with two parameterization scheme suites.

330 total rain outcomes. Previous study of comparing Thompson and WSM6 schemes found that the dominant size of graupel particles with Thompson scheme is larger than that with WSM6 scheme such that the different rainwater production and accompanied evaporative cooling below freezing level could be resulted (Bao et al., 2019). This may help explain the amplified evaporative cooling in the lower troposphere and intensified condensational warming in the upper troposphere (shown in Fig. 12) for simulations at 15km resolution with the CP scheme suite where the Thompson scheme is used, in contrast to the MS

335 scheme suite where the WSM6 scheme is used.

In order to show the smooth transition from coarse to fine resolution of the global variable-resolution simulation using the convection-permitting scale-aware scheme suite, we calculated the ~~parameterized, resolved~~ convective, grid-scale, and total precipitation along with the corresponding mesh spacing in the V3km.CP simulation (Fig. 15). As mentioned above, σ is set to 0.7 in the refined region (at the resolution of 3km) in V3km.CP simulation and this leads to the scaling factor $(1-\sigma)^2$=0.09

340 being multiplied by the maximum convective vertical eddy transport. It implies that only 9% of the cloud mass-flux-based parameterization of convection is utilized over the refined mesh region whereas the rest precipitation is computed from the

grid-scale precipitation. The comparison of the ~~parameterized precipitation against resolved~~ convective precipitation against grid-scale precipitation inside and outside the mesh refinement region clearly highlights the scale dependence of simulated precipitation upon the convective faction in the GF scheme. ~~In particular,~~ We found that the comparison between Fig. 15a and

345 Fig. 15b shows that as the spatial resolution transitions from 60km to 3km over the northern China, the convective precipitation significantly decreases while the ~~resolved~~ grid-scale precipitation increases. The increasing ~~resolved~~ grid-scale precipitation compensates smoothly decreasing ~~parameterized~~ convective precipitation over the area of mesh refinement, which means that the GF scheme accomplishes the remarkable scale-aware performance, enabling a continuous adjustment of the cloud mass flux based on the convective updraft fraction. Another interesting feature arising from Figure 15 is that the typhoon-associated

350 precipitation is clearly stratified as convective precipitation and grid-scale precipitation over the mesh transition area. As approaching to the refined region, more grid-scale precipitation can be found, which implies that the variable-resolution mesh could be an ideal too to study horizontal scale dependence of convective and grid-scale most processes associated with typhoons.

4.2 Spatial and Temporal Variation

355 Fig. 16 shows the meridional precipitation propagation over Henan province during the event. The CMA observation and the ERA5 reanalysis data show that the position of the rain belt moved northward from near 33°N on 19 July 00:00 UTC to 37°N on 22 July 00:00 UTC~~, with three peak periods of maximum precipitation intensity reaching its strongest point at 00:00 UTC on July 21. Fig. 16c-h present the model simulations with various resolutions and parameterization schemes.~~ . All simulations effectively predicted the northward movement of the precipitation pattern. ~~The performance of the CP~~

360 ~~parameterization scheme suite and the MS parameterization scheme suite at 15km is comparable. However, none of the simulations with CP parameterization scheme suite were able to effectively predict the 3rd peak, except for the~~ It is noteworthy that all CP simulations, including V3km.CP~~simulation. The U60km.MS simulation effectively captured the trend of northward movement of the precipitation location, but its simulated precipitation center at the 3rd peak is placed further north compared to~~, failed to simulate the precipitation from 21 July 12:00 to 22 July 06:00 UTC which can be characterized as the third

365 peak period. Nevertheless, this third peak period is accompanied with the least precipitation amount during this heavy rainfall event. Conversely, all MS aimulations, including QU60km.MS, captured the precipitation during the mentioned period, albeit with intensity deviations. In addition to the ~~observation. In addition, the performances of the 15km variable-resolution and quasi-uniform mesh are equivalent to each other with the same parameterization scheme suite. Among all simulations, V3km.CP simulation is closest to observations, as it effectively captures the three peaks and their timings are in the best agreement with~~

370 ~~observations. Moreover, the precipitation intensity simulated by V3km. CP is closest to observations.~~

~~In order to further evaluate the simulation performance of the rainfall location and intensity, we explore further by examining~~ meridional propagation of the precipitation phases investigated here, we also examined the simulated zonal propagation of rainfall over the Henan province from 20 July 00:00 to 22 July 00:00 UTC (Fig. 17). The precipitation mainly occurred at 113°E and there was a tendency for the precipitation to move eastward over time. ~~Similarly, there were three distinct peak~~

375 ~~periods, which are consistent with the results discussed earlier. Once again, both V15km.CP and V15km.MS simulations~~
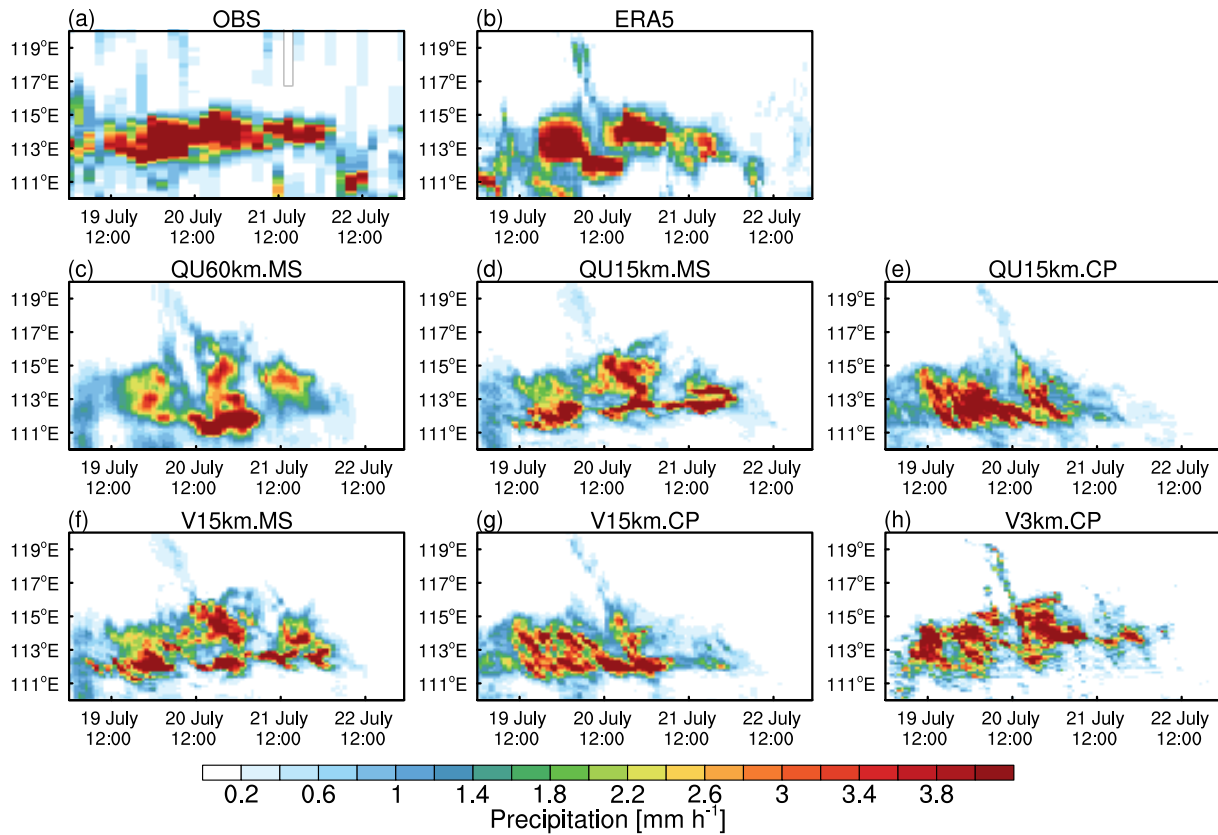
Figure 17. Time–longitude cross section of precipitation averaged over Henan province (30–40°N, 110–130°E) from the CMA station observations and the simulations with global uniform and variable-resolution with two schemes.

~~exhibit comparable forecast performance.~~ The precipitation forecasted by ~~U60km~~QU60km.MS was biased towards the east ~~,~~ ~~likely~~ due to the coarse resolution. ~~V3km.CP is closest to observation, in terms of both the predicted intensity and location, which is consistent with the results discussed above.~~ The forecast performance of the CP suite and MS suite at 15km is comparable for the first peak period, but the performance of the CP suite worsened for the second and third peak periods. In particular, all simulations with the CP suite at 15km missed the third peak indeed. While the precipitation locations predicted by the QU15km.MS and V15km.MS simulations exhibit a broader east-west spread compared to observation, the QU15km.CP and V15km.CP simulations incorrectly position the precipitation to the west and erroneously omit the precipitation during the third peak period.

380

5   Conclusion and discussion

385 This pioneering study introduces a novel modeling approach to predicting a historic rainstorm occurred over Henan province, China, in July 2021 ("7.20" extreme precipitation) by utilizing a global variable-resolution non-hydrostatic model (MPAS-Atmosphere). A global variable-resolution model (MPAS-Atmosphere v7.3) was employed to simulate this extreme precipitation event. A series of simulations have been done at both quasi-uniform (60km and 15km) and variable-resolution ~~meshes~~ (60-15km and 60-3km) meshes from hydrostatic to non-hydrostatic scale with two parameterization scheme suites. For the 48-hour

390 peak precipitation duration (07/20-07/22), the 60-3km variable-resolution simulation coupled with the scale-aware convection-permitting parameterization scheme suite stands out among all tested simulations as it reproduces this extreme precipitation event most accurately, in terms of both the intensity and location of the peak precipitation. At 15-km resolution, given the same parameterization schemes are selected, the 60-15km variable-resolution simulation achieves comparable forecasting skills as the 15-km quasi-uniform simulation, but with the former being performed at a much reduced computing cost. In

395 addition, we further compared two sets of built-in physical parameterization schemes, namely, the mesoscale suite and scale-aware convection-permitting suite, at quasi-uniform and variable-resolution mesh of ~~15 km respectively. We found that the~~ 15km respectively. The default mesoscale suite generally outperforms the convection-permitting suite ~~at 15-km resolution as both 15-km~~ in simulating precipitation at 15km resolution during the three peak periods of this event. In particular, both 15km quasi-uniform and 60-15km variable-resolution simulations coupled with convection-permitting parameterization

400 scheme suite missed the ~~3rd peak of the extreme precipitation event in contrast to simulations with mesoscale parameterization scheme suite. This implies that, when the resolution of the refined region is coarser than the cloud-resolving scale, the convection-permitting parameterization scheme suite does not necessarily work better than the default mesoscale suite, but once the refined mesh is close to the cloud-resolving scale, the convection-permitting suite becomes scale aware such that it can intelligently distinguish the convective precipitation and grid-scale precipitation, respectively~~third peak period which

405 is associated with least precipitation amount though. Hence, it is essential to match parameterization schemes with the grid resolution for optimal compatibility. Furthermore, ~~through this study, we also~~ we found that the large-scale ~~wind field plays a vital role in affecting the simulated extreme precipitation event since it largely influences the transport of the water vapor flux thereby altering the prediction of the precise peak precipitation location. Consequently, the latent heat release from the simulated peak precipitation would further feed back to~~ circulation plays a critical role in the peak precipitation simulations,

410 via influencing the simulated large-scale low-level wind. In specific, during the second 24-hour period, simulations with the convection-permitting parameterization scheme suite at 15km resolution are found to be associated with an easterly component wind bias in the lower troposphere relative to the default mesoscale suite. This easterly component wind bias is very likely due to the excessive evaporative cooling in the lower troposphere from the convection-permitting parameterization scheme suite in which the Thompson microphysics scheme is used whereas in the default mesoscale suite the WSM6 microphysics scheme is

415 used. In other words, at 15-km resolution, the diabatic heating associated with grid-scale precipitation largely accounts for the large-scale wind ~~field such that the impact of the wind field upon the simulated peak precipitation is amplified.~~ simulation bias such that this wind bias would, in turn, feedback to the total precipitation simulation bias.

Xu et al. (2023) used WRF with one-way nesting in simulating this same "7.20" extreme precipitation event, by setting the resolution of the outer domain at 20 km and inner domain at 4 km, respectively. They found that their simulations with GF convection scheme generate large bias from the observed precipitation field, whereas our global 60-3km variable-resolution simulation with the same GF convection scheme gives much improved prediction of the extreme precipitation location as well as intensity. This implies that the seamless mesh transition of the global variable-resolution model is superior in simulating the extreme precipitation event. In addition, Xu et al. (2023) found that the misrepresented large-scale circulation in the outer domain, due to the excessive latent heat simulated from the flawed convective parameterization scheme, could substantially impact the simulated peak precipitation over the inner domain. This is consistent with our results as we found that the large-scale wind field predominately influences the simulated peak precipitation in our MPAS simulations as well.

Moreover, in this study, we demonstrate that in the high-resolution simulation (3km), the total precipitation is primarily contributed by grid-scale precipitation, whereas in the low-resolution simulation (60km, 15km), the total precipitation is mainly influenced by subgrid-scale precipitation, which is also found by previous studies(Fowler et al., 2016; Zhao et al., 2019) . An evident characteristic is the smooth transition of grid-scale precipitation from the low-resolution region to the high-resolution region, which implies that the GF convective parameterization scheme is responsive to changes in resolution and promptly adjusts accordingly. These findings suggest that appropriate parameterization schemes need to be selected for different regions according to their respective grid scales. Furthermore, we emphasize the importance of considering the subgrid scale processes in precipitation simulations, as they play a significant role in the total precipitation, especially for simulations in refined areas.

Moreover, in this study, we demonstrate that for simulations at hydrostatic scale (60km), the convective precipitation is computed based on the equilibrium mass-flux-based parameterizations of convection with a scaling factor as 1, namely, the deep convection scheme. As the resolution is being pushed from the coarse to the intermediate level (15km), this scaling factor gradually decreases. For instance, for simulations at 15km, the scaling factor in front of the mass-flux-based convective scheme approximates to 0.8. When the resolution is pushed to the cloud-resolving scale (3km), the convective scheme becomes considerably small. For instance, for simulations with the variable-resolution mesh spanning between hydrostatic and non-hydrostatic scales (60-3km), the associated scale-aware GF convection scheme performs as a conventional deep convective scheme over the coarse region whereas it behaves as a shallow convective scheme over the refined region with the scaling factor becoming 0.09. Therefore, as the mesh resolution increases, the grid-scale precipitation becomes dominant in the total precipitation relative to the convective precipitation. Therefore, the MPAS variable-resolution meshes bridging hydrostatic and non-hydrostatic scales provide an excellent tool for evaluating the dependence of grid-scale and subgrid-scale precipitation upon horizontal resolutions.

For the conventional limited-area atmospheric model that is used for numerical weather prediction such as WRF, it has a number of longstanding issues including mismatching solution between outer domain and inner domain, wave reflection along imposed boundary of inner domain, and setting sponge zones next to lateral boundaries. So MPAS variable-resolution model provides an alternative way to bypass these issues as the simulations are done within an entire global framework. In addition, the scale-aware GF convection parameterization scheme makes it possible to quantify the scale-dependence of convective and grid-scale precipitation, even over the smooth transition-zone resolutions while the conventional limited-area model fails

on this aspect. Therefore, the analysis done in this study regarding the precipitation partitioning can be conducted in MPAS simulations of other extreme rainfall events similar to the July 20 event studied here. In addition, MPAS can be equally used

455 for typhoon simulations givens its excellent ability for investigating issue related to precipitation scale dependence.

The study of Xu et al. (2023) using WRF with one-way nesting at 20km/4km resolutions for the '7.20' event showed large biases in simulated precipitation with the GF convective scheme in contrast to the excellent simulation results by the 60-3km variable-resolution simulation performed in the present study. Nevertheless, both studies have found that the flawed convective parameterization scheme could lead to significant bias in the simulated large-scale circulation, thereby producing

460 biased precipitation simulation results. Moreover, in the current study, we have also found that the computed grid-scale precipitation based on different microphysics schemes may result in inaccurate diabatic heating and thus misrepresented large-scale circulation. Sun et al. (2023) diagnosed various mesoscale factors of the same "7.20" extreme precipitation event with a 4D data assimilation system and their results are consistent with what we found here in that this extreme precipitation event was maintained by the dynamical lifting of low-level converging flows from the south, southeast and the east of Henan

465 province. In addition, our study further elucidates how the easterly wind anomalies affect precipitation simulation bias. The specific topography may also be a key factor influencing this extreme rainfall event as Sun et al. (2023) and Yin et al. (2021) pointed out. Their study emphasized the role of the unique terrain of the Taihang and Funiu Mountains located to the west of Henan Province. Hence, their results are aligned with our findings in that the 60-3km variable-resolution simulation in the refined region can well capture the small details of these terrain effects.

470 This study found ~~the global 60km-3km~~ that the global 60-3km variable-resolution MPAS simulation coupled with scale-aware convection-permitting parameterization scheme suite outperforms alternative simulations, which is consistent with the previous studies (Zhao et al., 2019; Skamarock et al., 2018; Feng et al., 2018; Prein et al., 2015). ~~In addition, the resolved lower boundary forcings such as topography and surface heterogeneity exert~~ Sakaguchi et al. (2015) used the variable-resolution MPAS model, as a regional climate model, to simulate precipitation over East Asia and found that the surface heterogeneity

475 exerts significant influence on ~~regional precipitation simulations, signifying that the prediction of extreme precipitation events remains critical (Sakaguchi et al., 2015)~~the regional precipitation simulation, which is consistent with the role played by terrains in the extreme precipitation simulations. Endeavors aimed at ~~enhancing~~ improving the scale-aware function of convective parameterization may yield further advancements in the future (Gao et al., 2017; Hagos et al., 2013; Skamarock et al., 2012). Further study is ~~needed to investigate more quantitatively the sensitivity of the intensity and location of simulated~~

480 ~~extreme precipitation to the scaling factor in convection-permitting parameterization suite.~~ underway to investigate various variable-resolution meshes coupled with different convection schemes in simulating other extreme precipitation event.

Code and data availability. The exact version of the MPAS-A model along with all the data sets used in this study are available at Zenodo: https://zenodo.org/doi/10.5281/zenodo.10503571 (Liu et al., 2024). In addition, the model (MPAS-A v7.3) used is available from the project website: https://mpas-dev.github.io/ (last access: 14 January 2024). The global meshes generated for all the MPAS experiments in this study

485 can be downloaded from https://mpas-dev.github.io/atmosphere/atmosphere_meshes.html (last access: 14 January 2024). Hourly precipita-

tion, wind and temperature data from the European Centre for Medium-Range Weather Forecasts (ECMWF) Reanalysis can be downloaded from https://cds.climate.copernicus.eu/cdsapp#!/home (last access: 14 January 2024). Hourly surface observation data used in this study can be downloaded from https://data.cma.cn/ (last access: 14 January 2024).

Author contributions. LD and ZL designed the study and the experiments. LD, ZL, HY, DM, and XQ analyzed the simulations. XL pre-
490 pared and analyzed the observations. ZL, DL, and YW performed simulations and created the figures. All authors contributed to writing or discussing the manuscript.

Competing interests. The contact author has declared that none of the authors has any competing interests.

Acknowledgements. The authors thank European Centre for Medium-Range Weather Forecasts for providing datasets/models etc. All com-putations of this work were done at the Center for Computational Science and Engineering at Southern University of Science and Tech-
495 nology and we appreciate the high-quality service provided by the staff of this center. This work was supported in part by grants from the National Natural Science Foundation of China (Grant No. 41975060) and Shenzhen Science and Technology Program (Grant No. JCYJ20190809163007701 and JCY20200925160922002).

References

Arakawa, A. and Wu, C.-M.: A unified representation of deep moist convection in numerical modeling of the atmosphere. Part I, Journal of the Atmospheric Sciences, 70, 1977–1992, 2013.

Arakawa, A., Jung, J.-H., and Wu, C.-M.: Toward unification of the multiscale modeling of the atmosphere, Atmospheric Chemistry and Physics, 11, 3731–3742, 2011.

Bao, J.-W., Michelson, S. A., and Grell, E. D.: Microphysical Process Comparison of Three Microphysics Parameterization Schemes in the WRF Model for an Idealized Squall-Line Case Study, Monthly Weather Review, 147, 3093 – 3120, https://doi.org/https://doi.org/10.1175/MWR-D-18-0249.1, 2019.

Bechtold, P., Chaboureau, J.-P., Beljaars, A., Betts, A., Köhler, M., Miller, M., and Redelsperger, J.-L.: The simulation of the diurnal cycle of convective precipitation over land in a global model, Quarterly Journal of the Royal Meteorological Society: A journal of the atmospheric sciences, applied meteorology and physical oceanography, 130, 3119–3137, 2004.

Bechtold, P., Köhler, M., Jung, T., Doblas-Reyes, F., Leutbecher, M., Rodwell, M. J., Vitart, F., and Balsamo, G.: Advances in simulating atmospheric variability with the ECMWF model: From synoptic to decadal time-scales, Quarterly Journal of the Royal Meteorological Society: A journal of the atmospheric sciences, applied meteorology and physical oceanography, 134, 1337–1351, 2008.

Bechtold, P., Semane, N., Lopez, P., Chaboureau, J.-P., Beljaars, A., and Bormann, N.: Representing equilibrium and nonequilibrium convection in large-scale models, Journal of the Atmospheric Sciences, 71, 734–753, 2014.

Chen, F. and Dudhia, J.: Coupling an advanced land surface–hydrology model with the Penn State–NCAR MM5 modeling system. Part I: Model implementation and sensitivity, Monthly weather review, 129, 569–585, 2001.

Chen, F., Yuan, H., Sun, R., and Yang, C.: Streamflow simulations using error correction ensembles of satellite rainfall products over the Huaihe river basin, Journal of Hydrology, 589, 125 179, 2020.

Cheng, Y., Hui, P., Liu, D., Fang, J., Wang, S., Wang, S., and Tang, J.: MPAS-A Variable-Resolution Simulations for Summer Monsoon Over China: Comparison Between Global and Regional Configuration, Journal of Geophysical Research: Atmospheres, 128, e2022JD037 541, 2023.

Davis, C. A., Ahijevych, D. A., Wang, W., and Skamarock, W. C.: Evaluating medium-range tropical cyclone forecasts in uniform-and variable-resolution global models, Monthly Weather Review, 144, 4141–4160, 2016.

Ding, Y. and Johnny CL, C.: The East Asian summer monsoon: an overview, Meteorology and Atmospheric Physics, 89, 117–142, 2005.

Ding, Y., Wang, Z., and Sun, Y.: Inter-decadal variation of the summer precipitation in East China and its association with decreasing Asian summer monsoon. Part I: Observed evidences, International Journal of Climatology: A Journal of the Royal Meteorological Society, 28, 1139–1161, 2008.

Ding, Y., Liu, Y., and Hu, Z.-Z.: The record-breaking mei-yu in 2020 and associated atmospheric circulation and tropical SST anomalies, Advances in Atmospheric Sciences, 38, 1980–1993, 2021.

Du, Y. and Chen, G.: Heavy rainfall associated with double low-level jets over southern China. Part II: Convection initiation, Monthly Weather Review, 147, 543–565, 2019.

Feng, Z., Leung, L. R., Houze Jr, R. A., Hagos, S., Hardin, J., Yang, Q., Han, B., and Fan, J.: Structure and evolution of mesoscale convective systems: Sensitivity to cloud microphysics in convection-permitting simulations over the United States, Journal of Advances in Modeling Earth Systems, 10, 1470–1494, 2018.

Fowler, L. D., Skamarock, W. C., Grell, G. A., Freitas, S. R., and Duda, M. G.: Analyzing the Grell–Freitas convection scheme from
535   hydrostatic to nonhydrostatic scales within a global model, Monthly Weather Review, 144, 2285–2306, 2016.

Gao, Y., Leung, L. R., Zhao, C., and Hagos, S.: Sensitivity of US summer precipitation to model resolution and convective parameterizations
across gray zone resolutions, Journal of Geophysical Research: Atmospheres, 122, 2714–2733, 2017.

Grell, G. A. and Dévényi, D.: A generalized approach to parameterizing convection combining ensemble and data assimilation techniques,
Geophysical Research Letters, 29, 38–1, 2002.

540 Grell, G. A. and Freitas, S. R.: A scale and aerosol aware stochastic convective parameterization for weather and air quality modeling,
Atmospheric Chemistry and Physics, 14, 5233–5250, 2014.

Hagos, S., Leung, R., Rauscher, S. A., and Ringler, T.: Error characteristics of two grid refinement approaches in aquaplanet simulations:
MPAS-A and WRF, Monthly Weather Review, 141, 3022–3036, 2013.

Hong, S.-Y.: A new stable boundary-layer mixing scheme and its impact on the simulated East Asian summer monsoon, Quarterly Journal
545 of the Royal Meteorological Society, 136, 1481–1496, 2010.

Hong, S.-Y. and Lim, J.-O. J.: The WRF single-moment 6-class microphysics scheme (WSM6), Asia-Pacific Journal of Atmospheric Sci-
ences, 42, 129–151, 2006.

Hong, S.-Y., Noh, Y., and Dudhia, J.: A new vertical diffusion package with an explicit treatment of entrainment processes, Monthly weather
review, 134, 2318–2341, 2006.

550 Houze Jr, R. A.: Mesoscale convective systems, Reviews of Geophysics, 42, 2004.

Iacono, M. J., Mlawer, E. J., Clough, S. A., and Morcrette, J.-J.: Impact of an improved longwave radiation model, RRTM, on the energy
budget and thermodynamic properties of the NCAR community climate model, CCM3, Journal of Geophysical Research: Atmospheres,
105, 14 873–14 890, 2000.

Klemp, J. B.: A terrain-following coordinate with smoothed coordinate surfaces, Monthly weather review, 139, 2163–2169, 2011.

555 Klemp, J. B., Skamarock, W. C., and Dudhia, J.: Conservative split-explicit time integration methods for the compressible nonhydrostatic
equations, Monthly Weather Review, 135, 2897–2913, 2007.

Li, Z., Lau, W.-M., Ramanathan, V., Wu, G., Ding, Y., Manoj, M., Liu, J., Qian, Y., Li, J., Zhou, T., et al.: Aerosol and monsoon climate
interactions over Asia, Reviews of Geophysics, 54, 866–929, 2016.

Liang, Y., Yang, B., Wang, M., Tang, J., Sakaguchi, K., Leung, L. R., and Xu, X.: Multiscale Simulation of Precipitation Over East Asia by
560 Variable Resolution CAM-MPAS, Journal of Advances in Modeling Earth Systems, 13, e2021MS002 656, 2021.

Liu, B., Yan, Y., Zhu, C., Ma, S., and Li, J.: Record-breaking Meiyu rainfall around the Yangtze River in 2020 regulated by the subseasonal
phase transition of the North Atlantic Oscillation, Geophysical Research Letters, 47, e2020GL090 342, 2020.

Liu, Z., Dong, L., Qiu, Z., Li, X., Yuan, H., Meng, D., Qiu, X., Liang, D., and Wang, Y.: Global variable-resolution simulations of extreme
precipitation over Henan, China in 2021 with MPAS- Atmosphere v7.3, Zenodo [data set], https://doi.org/10.5281/zenodo.10503572,
565 2024.

Lonfat, M., Marks Jr, F. D., and Chen, S. S.: Precipitation distribution in tropical cyclones using the Tropical Rainfall Measuring Mission
(TRMM) Microwave Imager: A global perspective, Monthly Weather Review, 132, 1645–1660, 2004.

Nakanishi, M. and Niino, H.: An improved Mellor–Yamada level-3 model: Its numerical stability and application to a regional prediction of
advection fog, Boundary-Layer Meteorology, 119, 397–407, 2006.

570 Nakanishi, M. and Niino, H.: Development of an improved turbulence closure model for the atmospheric boundary layer, Journal of the
Meteorological Society of Japan. Ser. II, 87, 895–912, 2009.

Nie, Y. and Sun, J.: Moisture sources and transport for extreme precipitation over Henan in July 2021, Geophysical Research Letters, 49, e2021GL097 446, 2022.

Park, S.-H., Skamarock, W. C., Klemp, J. B., Fowler, L. D., and Duda, M. G.: Evaluation of global atmospheric solvers using extensions of the Jablonowski and Williamson baroclinic wave test case, Monthly Weather Review, 141, 3116–3129, 2013.

Prein, A. F., Langhans, W., Fosser, G., Ferrone, A., Ban, N., Goergen, K., Keller, M., Tölle, M., Gutjahr, O., Feser, F., et al.: A review on regional convection-permitting climate modeling: Demonstrations, prospects, and challenges, Reviews of geophysics, 53, 323–361, 2015.

Rao, J., Xie, J., Cao, Y., Zhu, S., and Lu, Q.: Record Flood-Producing Rainstorms of July 2021 and August 1975 in Henan of China: Comparative Synoptic Analysis Using ERA5, Journal of Meteorological Research, 36, 809–823, 2022.

Rauscher, S. A., Ringler, T. D., Skamarock, W. C., and Mirin, A. A.: Exploring a global multiresolution modeling approach using aquaplanet simulations, Journal of Climate, 26, 2432–2452, 2013.

Sakaguchi, K., Leung, L. R., Zhao, C., Yang, Q., Lu, J., Hagos, S., Rauscher, S. A., Dong, L., Ringler, T. D., and Lauritzen, P. H.: Exploring a multiresolution approach using AMIP simulations, Journal of Climate, 28, 5549–5574, 2015.

Skamarock, W. C. and Gassmann, A.: Conservative transport schemes for spherical geodesic grids: High-order flux operators for ODE-based time integration, Monthly Weather Review, 139, 2962–2975, 2011.

Skamarock, W. C. and Klemp, J. B.: A time-split nonhydrostatic atmospheric model for weather research and forecasting applications, Journal of computational physics, 227, 3465–3485, 2008.

Skamarock, W. C., Klemp, J. B., Duda, M. G., Fowler, L. D., Park, S.-H., and Ringler, T. D.: A multiscale nonhydrostatic atmospheric model using centroidal Voronoi tesselations and C-grid staggering, Monthly Weather Review, 140, 3090–3105, 2012.

Skamarock, W. C., Duda, M. G., Ha, S., and Park, S.-H.: Limited-area atmospheric modeling using an unstructured mesh, Monthly Weather Review, 146, 3445–3460, 2018.

Skamarock, W. C., Snyder, C., Klemp, J. B., and Park, S.-H.: Vertical resolution requirements in atmospheric simulation, Monthly Weather Review, 147, 2641–2656, 2019.

Sun, J., LI, R., Zhang, Q., Trier, S. B., Ying, Z., and Xu, J.: Mesoscale factors contributing to the extreme rainstorm on 20 July 2021 in Zhengzhou, China as revealed by rapid update 4DVar analysis, Monthly Weather Review, 2023.

Sun, R., Yuan, H., and Yang, Y.: Using multiple satellite-gauge merged precipitation products ensemble for hydrologic uncertainty analysis over the Huaihe River basin, Journal of Hydrology, 566, 406–420, 2018.

Sun, W., Mu, X., Song, X., Wu, D., Cheng, A., and Qiu, B.: Changes in extreme temperature and precipitation events in the Loess Plateau (China) during 1960–2013 under global warming, Atmospheric Research, 168, 33–48, 2016.

Thompson, G. and Eidhammer, T.: A study of aerosol impacts on clouds and precipitation development in a large winter cyclone, Journal of the atmospheric sciences, 71, 3636–3658, 2014.

Thompson, G., Field, P. R., Rasmussen, R. M., and Hall, W. D.: Explicit forecasts of winter precipitation using an improved bulk microphysics scheme. Part II: Implementation of a new snow parameterization, Monthly Weather Review, 136, 5095–5115, 2008.

Tiedtke, M.: A comprehensive mass flux scheme for cumulus parameterization in large-scale models, Monthly weather review, 117, 1779–1800, 1989.

Wang, B., Xiang, B., and Lee, J.-Y.: Subtropical high predictability establishes a promising way for monsoon and tropical storm predictions, Proceedings of the National Academy of Sciences, 110, 2718–2722, 2013.

Wang, W.: Forecasting Convection with a "Scale-Aware" Tiedtke Cumulus Parameterization Scheme at Kilometer Scales, Weather and Forecasting, 37, 1491–1507, 2022.

610   Wicker, L. J. and Skamarock, W. C.: An Implicit–Explicit Vertical Transport Scheme for Convection-Allowing Models, Monthly Weather Review, 148, 3893–3910, 2020.

Xu, H., Duan, Y., and Xu, X.: Indirect Effects of Binary Typhoons on an Extreme Rainfall Event in Henan Province, China From 19 to 21 July 2021: 1. Ensemble-Based Analysis, Journal of Geophysical Research: Atmospheres, 127, e2021JD036 265, 2022.

Xu, M., Zhao, C., Gu, J., Feng, J., Hagos, S., Leung, L. R., Luo, Y., Guo, J., Li, R., and Fu, Y.: Convection-Permitting Hindcasting of Diurnal
615   Variation of Mei-yu Rainfall Over East China With a Global Variable-Resolution Model, Journal of Geophysical Research: Atmospheres, 126, e2021JD034 823, 2021.

Xu, M., Zhao, C., Gu, J., Feng, J., Li, G., and Guo, J.: Appropriately representing convective heating is critical for predicting catastrophic heavy rainfall in 2021 in Henan Province of China, Environmental Research Communications, 2023.

Yin, J., Gu, H., Liang, X., Yu, M., Sun, J., Xie, Y., Li, F., and Wu, C.: A possible dynamic mechanism for rapid production of the extreme
620   hourly rainfall in Zhengzhou City on 20 July 2021, Journal of Meteorological Research, 36, 6–25, 2021.

Zhai, P., Zhang, X., Wan, H., and Pan, X.: Trends in total precipitation and frequency of daily precipitation extremes over China, Journal of climate, 18, 1096–1108, 2005.

Zhang, C., Wang, Y., and Hamilton, K.: Improved representation of boundary layer clouds over the southeast Pacific in ARW-WRF using a modified Tiedtke cumulus parameterization scheme, Monthly Weather Review, 139, 3489–3513, 2011.

625   Zhang, M. and Meng, Z.: Warm-sector heavy rainfall in southern China and its WRF simulation evaluation: A low-level-jet perspective, Monthly Weather Review, 147, 4461–4480, 2019.

Zhao, C., Leung, L. R., Park, S.-H., Hagos, S., Lu, J., Sakaguchi, K., Yoon, J., Harrop, B. E., Skamarock, W., and Duda, M. G.: Exploring the impacts of physics and resolution on aqua-planet simulations from a nonhydrostatic global variable-resolution modeling framework, Journal of Advances in Modeling Earth Systems, 8, 1751–1768, https://doi.org/https://doi.org/10.1002/2016MS000727, 2016.

630   Zhao, C., Xu, M., Wang, Y., Zhang, M., Guo, J., Hu, Z., Leung, L. R., Duda, M., and Skamarock, W.: Modeling extreme precipitation over East China with a global variable-resolution modeling framework (MPASv5.2): impacts of resolution and physics, Geoscientific Model Development, 12, 2707–2726, https://doi.org/10.5194/gmd-12-2707-2019, 2019.

Zheng, J. and Wang, C.: Influences of three oceans on record-breaking rainfall over the Yangtze River Valley in June 2020, Science China Earth Sciences, 64, 1607–1618, 2021.